

T-Junction experiment

ADVANCED PHYSICS LABORATORY

Academic year 2020/21

FINAL LABORATORY REPORT

ALESSANDRA SABATTI

ALESSANDRO LOVO

MARCO FERRARI

March 5, 2021

Contents

1	Introduction	1
1.1	Goals of the experiment	1
1.2	Physics of the droplet generation	1
2	Experimental apparatus	2
3	Data collection	6
4	Data Analysis	8
4.1	Electronic signals analysis	8
4.1.1	Shape of the Waveforms	8
4.1.2	Re-sampling of the signals	11
4.1.3	Fast Fourier Transform filter	11
4.1.4	Straightening of the signals	11
4.1.5	Identification of the droplet edges	13
4.1.6	Errors of measurement	14
4.1.7	Droplet characterization	15
4.2	Videos	18
4.2.1	Image preprocessing	18
4.2.2	Waveform extraction	19
4.2.3	Finding the droplets edges	19
4.2.4	Identifying the droplets	21
4.2.5	Droplet statistics	21
5	Results	23
6	Conclusion	27

1 Introduction

1.1 Goals of the experiment

The aim of this report is the characterization of the generation of water droplets in a continuous oil phase by a microfluidic device using sub-millimeter sized channels in a T-junction geometry. The droplets parameters, such as frequency, size and velocity, are measured by means of an electronic photocell tracking circuit and with the analysis of videos of the droplets flow acquired with a microscope camera.

1.2 Physics of the droplet generation

Flows of fluids in microfluidic systems are usually characterized by low values of the Reynolds number ($Re = \rho ul/\mu$, where ρ and μ are respectively the density and dynamic viscosity of the fluid, u the speed of flow, and l the characteristic dimension of the system). [1] This means that the Navier-Stokes equation for fluid flow becomes linear and the flow is laminar. However, the interaction between two immiscible fluids introduces non-linearity and instability in the microfluidic device, [2] which leads to the formation of droplets.

In the T-junction device, the principal channel carries the continuous phase (mineral oil) and the orthogonal channel is the inlet for the fluid that will form the dispersed phase (colored water). The process of drop formation can be explained as follows: at first the two immiscible fluids form an interface where the inlet connects to the

main channel; then the stream of the dispersed phase penetrates into the main channel and a droplet begins to grow. As the pressure gradient and the flow in the main channel distort the droplet in the downstream direction, the interface on the upstream side of the droplet moves downstream. When the interface approaches the downstream edge of the inlet for the dispersed phase, the neck connecting the inlet channel with the droplet breaks, releasing the droplet into the main channel. As this happens the tip of the stream of the dispersed phase snaps back to the edge of the inlet and the process repeats. [1] This breakup process can be described as the result of three forces: surface tension, shear-stress, and the force arising from the increased resistance to the flow in the main channel caused by the forming droplets. [1]

2 Experimental apparatus

The experimental setup is schematically reported in figure 1.

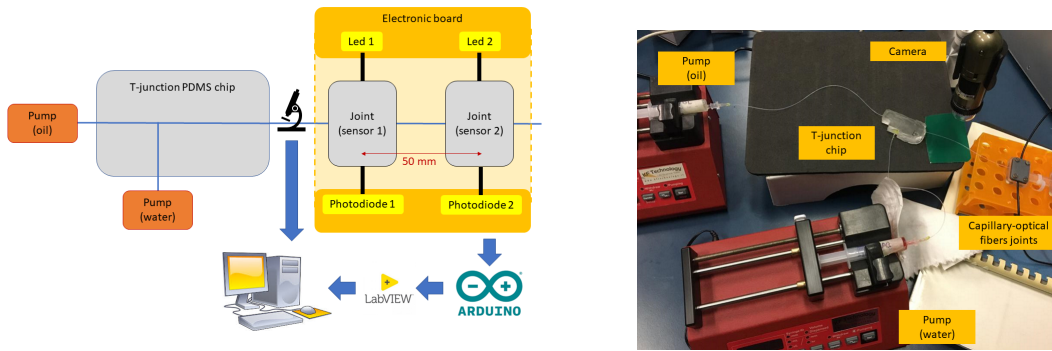


Figure 1: The whole experimental setup

Two syringe pumps, KF Technology model NE-300, are connected with two capillaries with an internal diameter of $300\text{ }\mu\text{m}$ to the T-junction chip. By tuning the flow rates of the pumps it is possible to control the size and the frequency of the droplets generated in the junction. The chip forming the T-junction has been realized in polydimethylsiloxane (PDMS) with the standard technique in two separate components, which then were treated with oxygen plasma in order to stick them together creating the microfluidic channels. The two parts were obtained from two molds realized with a stereolithography (SLA) 3D printer (see figures 2 and 3). In order to understand how the geometry of the channels affects the droplet generation process we built two different chips:

- A The straight channel from the oil input to the output has a square cross section with side of $300\text{ }\mu\text{m}$ while the water input has a vertical side of $300\text{ }\mu\text{m}$ and a horizontal one of $200\text{ }\mu\text{m}$. The input capillaries are connected to the chip by poking it from the upper face, thus entering orthogonal to the channels.
- B The oil input has a square cross section with side of $500\text{ }\mu\text{m}$ and 15 mm after the junction it smoothly shrinks to a square cross section with side of $300\text{ }\mu\text{m}$, in order to gently adapt to the output capillary, thus preventing the droplets from breaking. The water input has a vertical side of $500\text{ }\mu\text{m}$ and a horizontal one of $400\text{ }\mu\text{m}$. For this chip instead the input capillaries enter coaxially with the channels.

The output capillary (as usual with internal diameter of $300\text{ }\mu\text{m}$) passes under a microscope camera and then through a system of two photocells kept at a distance of 50 mm (see figure 5).

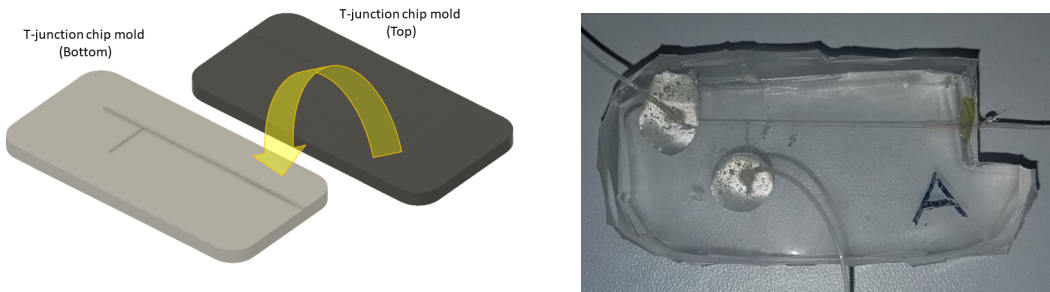


Figure 2: 3D Model of the mold (left) and the chip A in PDMS (right)

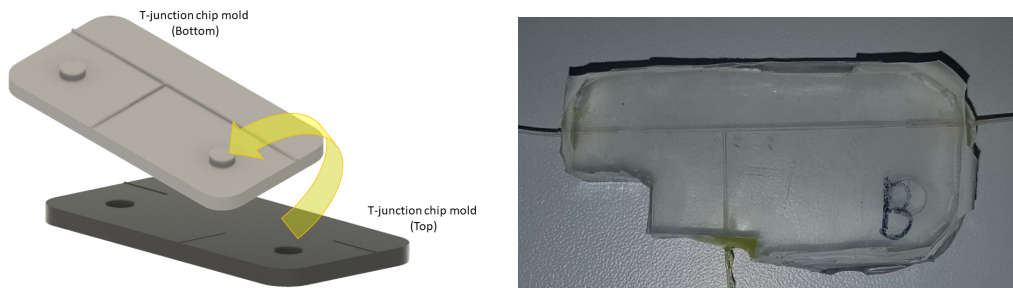


Figure 3: 3D Model of the mold (left) and the chip B in PDMS (right)

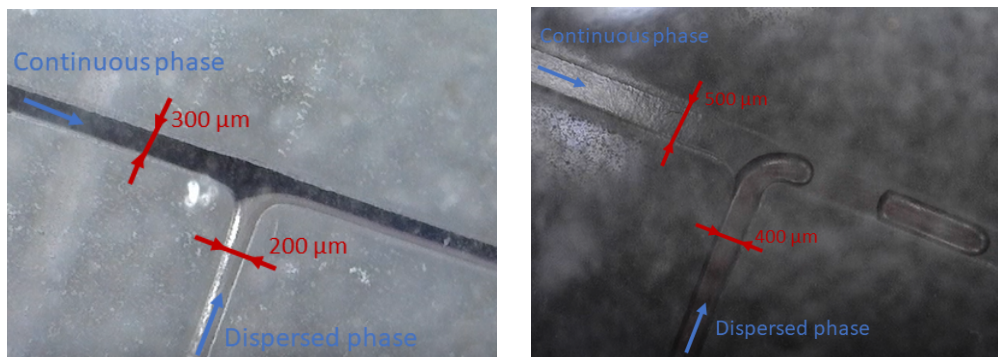


Figure 4: A magnification of the T-junction: chip A on the left (continuous phase ink, dispersed phase water: since they are miscible there is no droplet generation), chip B on the right (continuous phase oil, dispersed phase water: droplet generation)

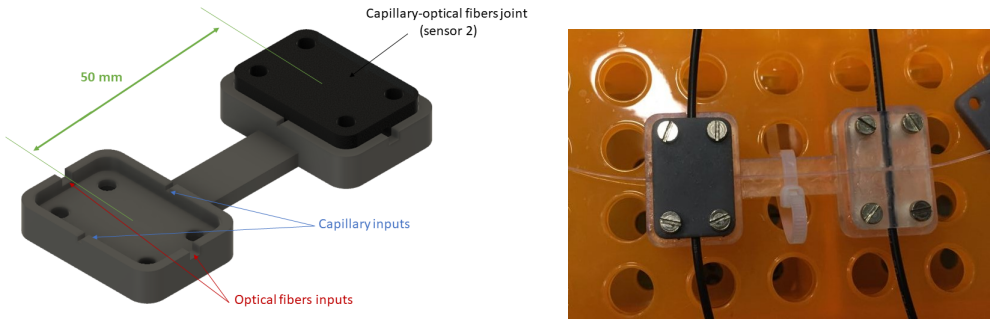


Figure 5: 3D Model of the joints holder (left) and the printed and assembled components (right)

As shown in figure 6 the photocell system is composed by a joint of two optical fibers (1 mm of internal diameter) facing each other with the capillary in between them. The light of a LED is coupled into one optical fiber, then it passes through the capillary, where it is altered by the presence of the droplets and then it is collected by the second optical fiber and delivered to an OPT101 photodiode, which produces an electronic signal proportional to the light intensity reaching it, which is then amplified by an electronic circuit (see below).

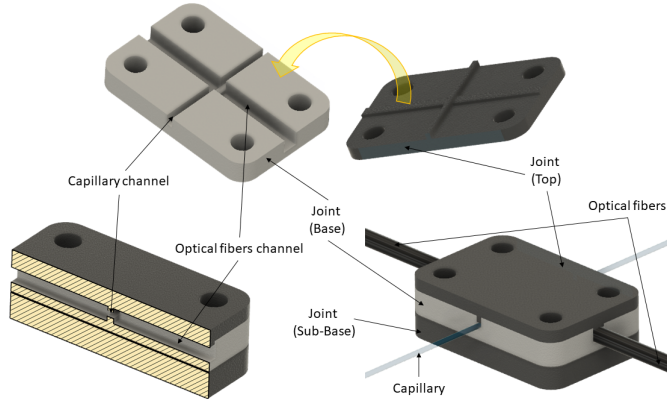


Figure 6: 3D Model of the capillary-optical fibers joint for the drops detection system

The coupling of the optical fibers with the electronic board is achieved via four components 3D-printed with SLA technology (two for each photocell system). These components include a bolt/nut system in order to keep the optical fibers in place, avoiding possible movements or detachments (see figure 7) and are then bolted to the electronic board. The two LED supports are printed in transparent resin, while the two for the photodiodes are painted black to properly shield them from the ambient light.

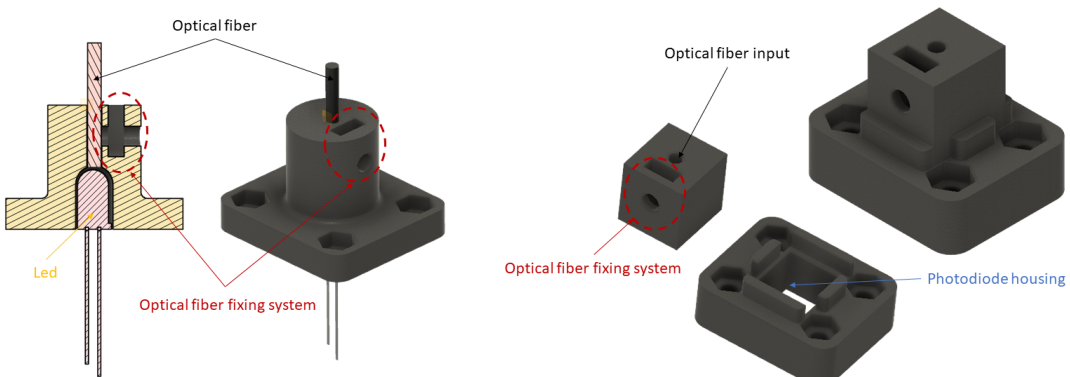


Figure 7: 3D Models of the LED and the photodiode holders. For the latter the two pieces are glued together.

In figure 8 are reported two views of the electronic board.

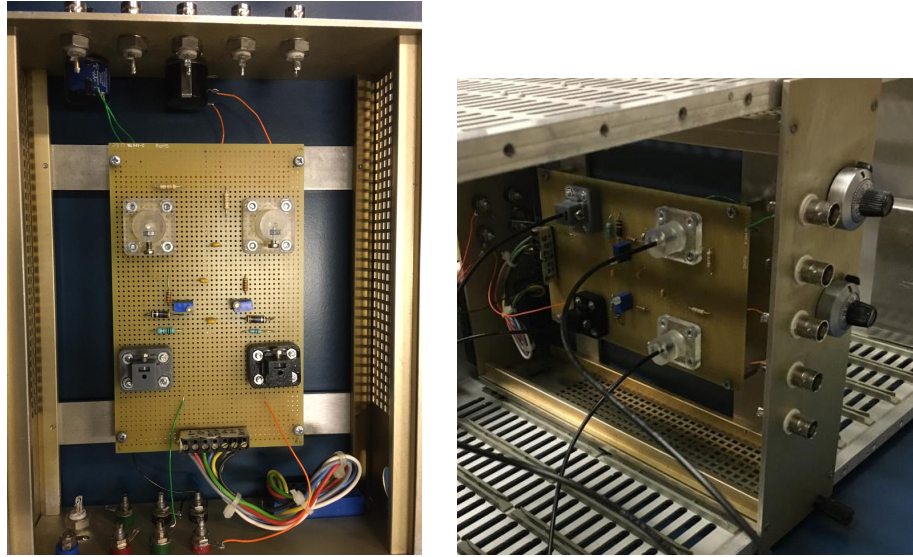


Figure 8: Top view of the electronic board (left) and once connected to the optical fibers and the power supply

The electronic board is assembled into a NIM module and connected to a power supply that provides a ground pin and a $V_{cc} = 6V$ DC pin.

LED circuit From the specifics of the LED the maximum current that can flow through the LED is $I_{max} = 20\text{mA}$ while the typical voltage drop across the LED is $V_x \approx (2.2 - 2.5)\text{V}$. Considering that we want to use as variable resistor RV_2 the helipot of the NIM module, that has a maximum resistance of $P = 100\Omega$, one can write the following:

$$I = \frac{V_{cc} - V_x}{R_4 + Px} < I_{max}$$

Where $x \in [0, 1]$ and Px is the resistance between pin 1 and 2 of the helipot. This allows to properly choose the value of the resistor $R_4 \approx 180\Omega$. By checking with an amperometer the current flowing through the LED, we measured a current ranging from 13mA for $x = 1$ to 20mA for $x = 0$, confirming that everything works properly.

It is important to notice that pin 3 of the helipot isn't connected to anything (figure 9).

Photodiode circuit Let's consider the variable resistor RV_1 to have a total resistance of P and a resistance of Px between pins 2 and 3. If we shield the photodiode and consider $x = 0$, the circuit acts as a simple non inverting amplifier with a gain factor $g = 1 + \frac{R_2}{R_1} \approx 6$ considering $R_1 \approx 10M\Omega$ and $R_2 \approx 50M\Omega$. If now we vary x , we can notice that if $P, R_3 \ll R_1$, we can use the simple formula of the voltage divider: if we call V_x the voltage of pin 2 of the variable resistor we get

$$V_x = V_{cc} \frac{P}{P + R_3} x$$

which adds an offset term to the output voltage:

$$V_{offset} = -\frac{R_2}{R_1} V_x = -V_{cc} \frac{R_2 P}{R_1 (P + R_3)} x$$

that allows to zero out the effect of the small amount of ambient light that manages to reach the photodiode. To select a proper value for R_3 and P we imposed $V_{offset} \in [-V_{cc}, 0]$, that lead us to choose $P = 10k\Omega$ and $R_3 \approx 35k\Omega$.

Capacitors C_1 and C_2 with a value of 470nF remove high frequency oscillations from the power supply, stabilizing the circuit.

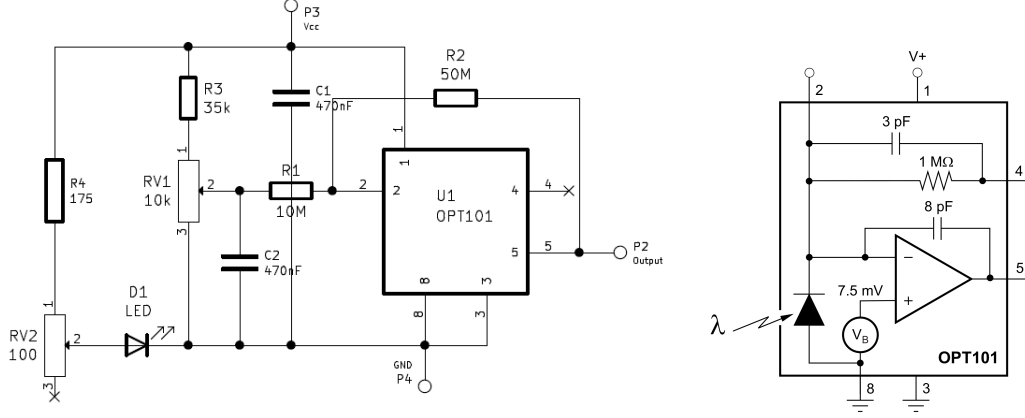


Figure 9: Photodiode and led electronic circuit and internal circuit of the OPT101 photodiode.

Data collection system The two outputs of the electronic board (one for each photocell) are connected to two analog inputs of an Arduino board which samples the electric signals every $dt = 10\text{ms}$ (actually the real dt is quite longer, see 4.1.2 for more details). The analog to digital conversion (ADC) is done using 10 bits over a 5V of signal range, i.e. having a voltage resolution of $\frac{5}{1024} = 4.88\text{mV}$. The signals so digitized are then sent (together with the timestamp of the measurement) to a LabView interface to plot a live graph of the behavior of the two signals. Then the collected data are saved to a spreadsheet.

Microscope To collect the videos of the droplets we used a *Dino-Lite* camera, which is provided with a knob to adjust focus and magnification of the image, with some white LEDs around the lens to illuminate the subject and a polarizing filter that can be rotated to prevent the reflected LED light from entering the camera and thus saturating the pixels.

The program for video acquisition allows to tune common settings for a camera like saturation or brightness, and allows to take single pictures, a video (at 10 fps (frames per second)) or a timelapse taking a picture at regular intervals of at least 1 second. However, as will be discussed more in the data analysis section, the actual time interval between frames is far from being constant, impairing consistently the measurements. In the program there is also the option of calibrating the images with a known length, however when the video is saved, this calibration is lost. For this reason we decided to include in the field of view of the camera a small ruler and to calibrate the images during data analysis.

We put the camera roughly 5 cm above the capillary, oriented in such a way to have it lying on the diagonal of the frames, in order to maximize the length observed. Furthermore, to increase the contrast of the pink-reddish droplets with respect to the background we tried putting below the capillary white, green or black paper, and the white one gave us the best results.

3 Data collection

Each dataset (characterized by the chip used (A or B) and the oil and water fluxes) consists of a timelapse of the droplets moving in the capillary, captured by the camera; and of a spreadsheet with the voltage readings of the two photodiodes and the timestamps of the measurements.

Nominally the timelapse has frames spaced every spf (most of the time we set $spf = 1\text{s}$), and the voltage readings are performed every dt that for almost every dataset is set to $dt = 10\text{ ms}$. However, as will be explained in more details later, due probably to some bugs in the recording softwares or to the poor performances of the lab computer, both spf and dt vary quite a lot during the acquisition.

Anyways, when collecting the data one has to set reasonable values for the two fluxes and the acquisition time. To do so one can do some rough computations: if we call respectively q_w and q_o the water and oil fluxes (volume over time) and $q = q_w + q_o$, and calling ϕ the inner diameter of the capillary one can have a first

estimate of the droplets velocity. Considering the two fluids as incompressible and unmiscible, one can write

$$v = \frac{q}{\frac{\pi}{4}\phi^2} \rightarrow v|_{[\text{mm/s}]} = 0.236(q|_{[\mu\text{L/min}]})$$

As can be seen from figure 10 for chip A the distance between the beginning of a droplet and the beginning of the next one is $\lambda_A \approx 1\text{mm}$, while for chip B $\lambda_B \approx 7\text{mm}$. Now, if we want to have a quite good resolution on the electronic signal one can say that there should be at least n_{min} sample points in the space λ , which can be expressed as

$$n = \frac{\lambda}{vdt} > n_{min} \rightarrow v < v_{max} := \frac{\lambda}{n_{min}dt}$$

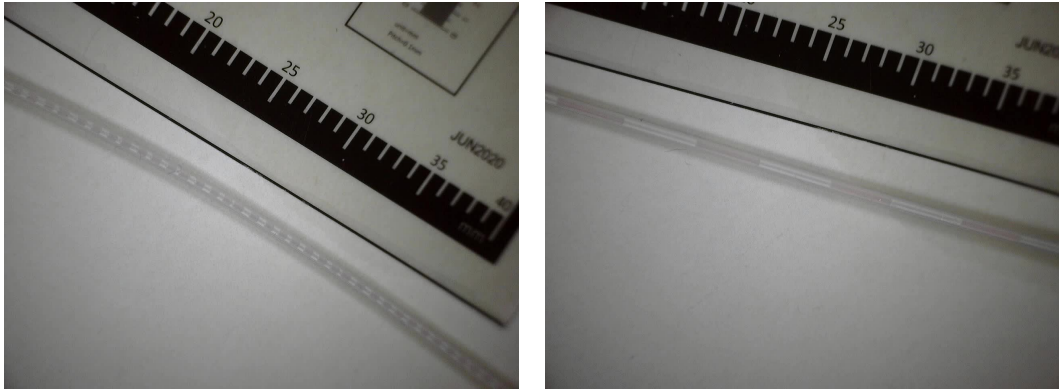


Figure 10: Example of two frames from timelapses respectively with chip A and B; notice the ruler for calibrating the images.

If now we consider $dt = 10\text{ ms}$ and, for instance, $n_{min} = 100$ and we assume that λ does not depend very much on q (as will be verified in section 5), we get $v_{max}^A = 1\text{ mm/s}$, $v_{max}^B = 7\text{ mm/s}$, and hence, using the previous relation, $q_{max}^A \approx 4\text{ }\mu\text{L/min}$ and $q_{max}^B = 30\text{ }\mu\text{L/min}$. Notice that, since the field of view of the camera contains roughly 30 mm of capillary and assuming $spf = 1\text{ s}$, this constraint on the velocities also implies that every droplet should appear in each frame roughly at least 30 times for chip A and 4 times for chip B.

Now to estimate the appropriate total time T a measurement campaign should take, one can consider a typical number of droplets $N = 200$ to observe, so

$$N = \frac{Tv}{\lambda} \rightarrow T = \frac{\lambda N}{v} \rightarrow T|_{[\text{s}]} \approx 850 \frac{\lambda|_{[\text{mm}]}}{q|_{[\mu\text{L/min}]}}$$

At this point all the parameters of each measurement can be properly set. However, datasets with very low flow rates would require a lot of time to record, so for those we simply observed less droplets.

There is one last thing to consider: since all droplets look very similar it is very difficult in the electronic signal to correctly identify the two appearances of the same droplet in the two detectors, namely it is difficult to measure the velocity of the droplets. The workaround we adopted is to first fill the capillary with oil only by keeping the water syringe pump off; then, turn it on and start the acquisition before the droplets reach the detectors. This way it is immediate to identify the droplets.

In figure 11 it is reported an example of the signals output of the two photocells electronic circuit. The voltage is low when oil flows in the capillary and rises every time a water droplet passes by.

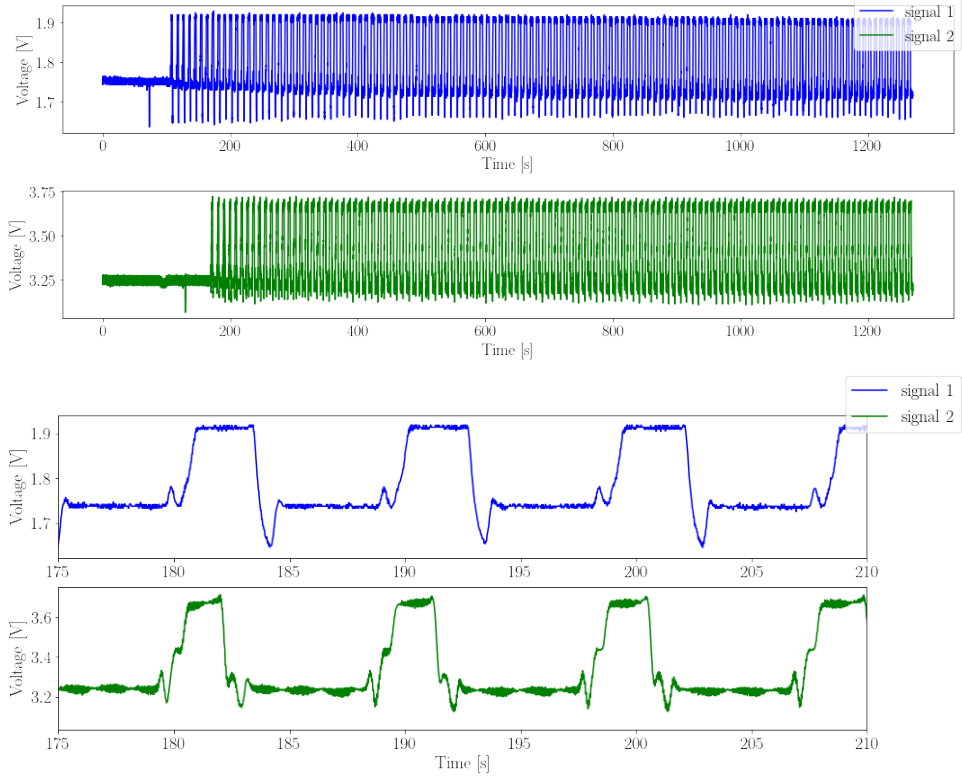


Figure 11: Example of the photocells system output signals. Acquisition with $q_w = q_o = 2 \mu\text{L}/\text{min}^2$. The first two plots are the whole acquisition, while the second two are a highlight of the shape of the droplets.

4 Data Analysis

The data analysis is performed combining the processing of the pictures acquired with the microscope and the analysis of the electrical signals of the photocells system.

From the first one it will be possible to determine directly the spatial size and distance distribution of the droplets but not their temporal ones. This is due to the rate of the microscope acquisitions, which is not constant.

From the electronic analysis, instead, the frequency of droplets generation and their velocity will be estimated.

4.1 Electronic signals analysis

4.1.1 Shape of the Waveforms

Before starting with the data analysis, in order to understand the shape of the electrical signals, we have done a ray tracing simulation of the interaction between the capillary, the fluid flowing in it, and the two optical fibers. The refractive indexes of the capillary, water and oil are respectively $n_c = 1.36$, $n_w = 1.33$ and $n_o = 1.467$.

First of all we considered how the circularity of the capillary affects light transmission when different fluids are inside it by considering a cross section of the capillary, which has outer diameter of $600 \mu\text{m}$ and inner diameter of $300 \mu\text{m}$, and assuming rays of light from the optical fiber are parallel and lie on the plane of the cross section. From the figure on the left we can see that, when there is air in the capillary, light rays are deflected

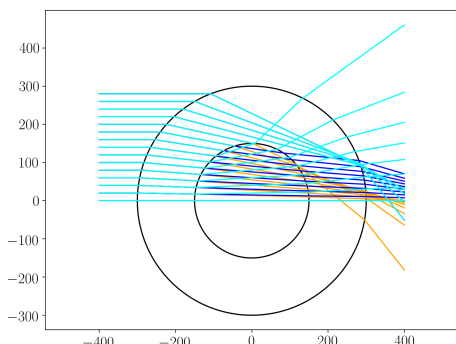


Figure 12: Lens effect of the capillary filled with air (cyan), oil (orange) and water (blue)

upwards, out of the collection zone, explaining why we experimentally observe a very low electronic signal. On the other hand, with water, light is properly focused on the second optical fiber, while, with oil, light is focused before the optical fiber and so the effect is a lower signal with respect to the water one. In simpler terms water matches the refractive index of the capillary and so light rays are deflected less.

So, if the droplets had no menisci we would expect a trapezoidal waveform, where the amount of collected light transitions roughly linearly between the oil and water levels, as the drop edge moves through the beam of light.

However the experimental waveform is much more complex and to explain it we resorted to another simplified 2D model: we considered the equatorial section of the capillary between the inner walls, assuming that the light beam coming from the first optical fiber has a divergence of $\pi/6$ while the droplet has circular menisci with size of $70\text{ }\mu\text{m}$ for the forward one and $30\text{ }\mu\text{m}$ for the backward one (these parameters are the ones that yield results most similar to the experimental waveforms). For simplicity we neglected here the effect of the walls of the capillary and its circularity (since we are in the equatorial plane) and also assumed that the equatorial plane of the capillary is also the equatorial plane of the optical fibers. Due to these simplifications the simulated waveform will not display significantly different water and oil levels but will instead focus on the effect of the menisci.

In figure 13 are reported the experimental waveforms of the two photocell signals for the same droplet (in the lower right) and the configurations of the optical fibers/capillary junction at salient positions x of the front edge of the droplet (pictures from 1 to 11); the droplet is represented in blue, and the green trapezoid represents light exiting from fiber 1 (on top of the capillary in the pictures) and spreading towards fiber 2 (on the bottom). Superimposed to these configurations it is plotted the simulation of the intensity profile on the bottom wall of the capillary, while in the title relative to each configuration it is reported the total intensity I_{tot} collected by the second optical fiber. By plotting I_{tot} as a function of x we obtained the results in figure 14.

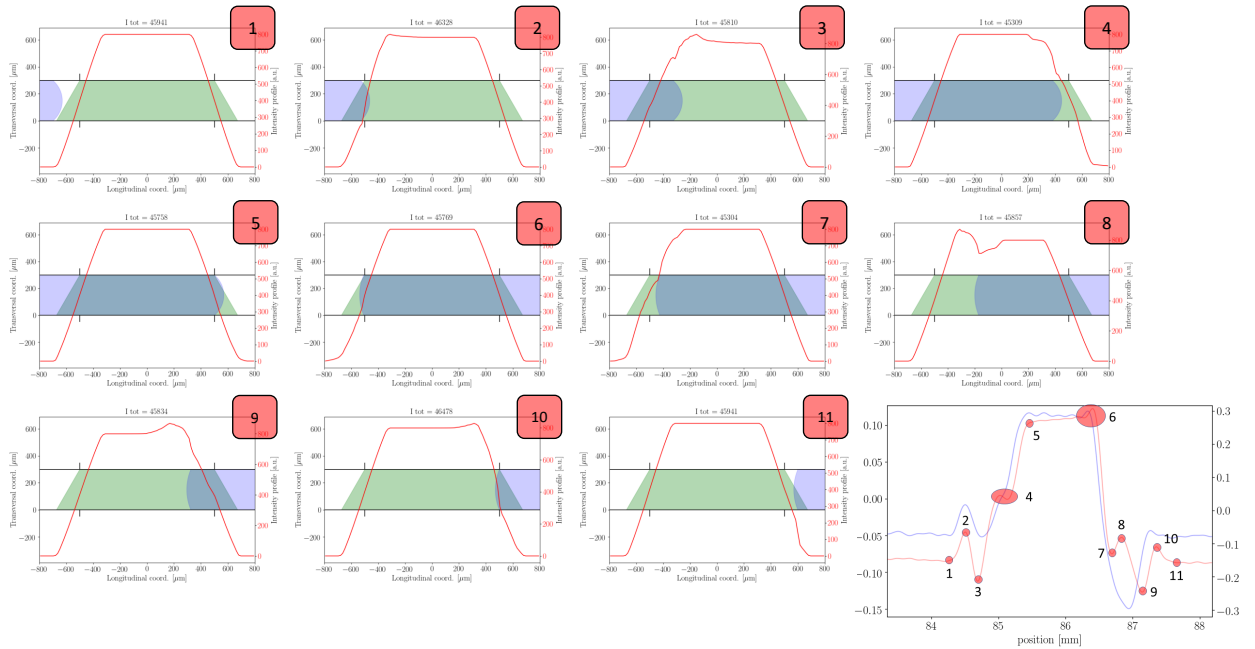


Figure 13: Visualization of the effect of the menisci on the transmitted light profile and example of experimental waveforms collected by the two photocells.

From the simulated intensity profiles we can see that the main effect of a meniscus is reflecting light in the region just outside the droplet (point 6 is an exception). So we deduced the following fundamental steps of the droplet flow across the photocell system. At first the water droplet is sufficiently far from the optical fiber, so the electronic signal is equal to the oil phase level (1). As the drop approaches, the forward meniscus reflects a

portion of light that wouldn't have been collected into the collection area, resulting in the first intensity peak. After the meniscus reaches the optical fiber (2), this effect is lost and the signal decreases to just below the oil level (3). As the forward meniscus approaches the right edge of the fiber, this time it reflects some light out of the collection area, thus slowing the linear increase in intensity due to the transition between the oil and water levels (4). This effect is more pronounced in the second photocell, where it creates a proper dip in the waveform, while for the first photocell it just shows up as a shoulder. Subsequently, when the water droplet fills the entire photocell area, the signal saturates to the water level (5). Then, the backward meniscus reflects a small amount of light into the collection area causing a tiny peak at the end of the water level (6). Notice that, as reported in the simulations in figure 14, this peak is more pronounced the smaller the meniscus size, and in particular it is not visible at all if the backward meniscus is larger than 50 μm ; this is the reason why we do not observe a peak at point (5), as the forward meniscus is bigger than the backward one. After that, the oil phase starts to fill again the photocell area and so the luminosity decreases. Due to the backward meniscus, which reflects the light out of the photocells area, this decrease is initially very steep (7). When the meniscus is sufficiently inside the optical fiber range, this effect stops and a change in the slope occurs (8). In this particular configuration we can fully appreciate the effect of the meniscus, namely 'moving' some intensity in the region inside the droplet to its immediate outside. The luminosity keeps decreasing until the backward meniscus reaches the end of the optical fiber (9). Now the droplet exits the photocell and some rays, which were directed outside the optical fiber, are reflected back due to the backward meniscus (10). Finally, the droplet is far away from the photocell system and the signal settles to the oil phase level (11).

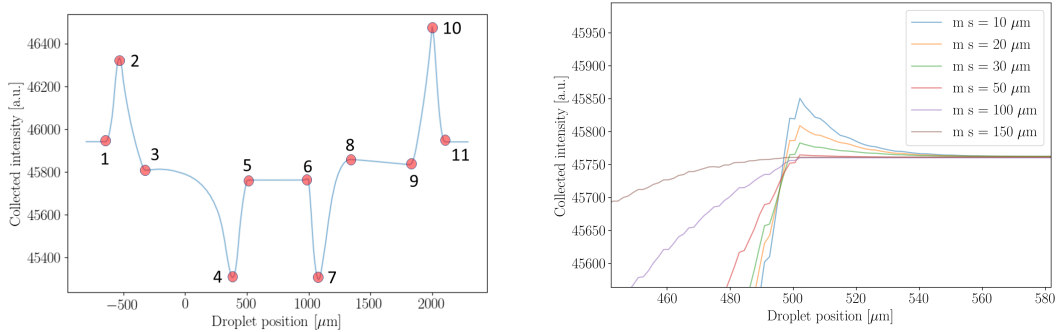


Figure 14: A simulated waveform as a function of the droplet position in the joint (left) and the magnification of the peak 6 (the x axis here is reversed and with an offset) for various sizes of the backward meniscus

Consequences on droplet edges identification This study on the signal shape was useful for understanding the actual drop position in the channel as a function of the voltage variation in the signal pattern, as to correctly define the droplet edges. In particular we define four of them:

- **Wide start (s_w)**: point 2, first peak in the waveform: the forward meniscus is at the upstream edge of the optical fibers
- **Narrow start (s_n)**: point 5, start of the water level: the forward meniscus is at the downstream edge of the optical fibers
- **Narrow end (e_n)**: point 6, end of the water level: the backward meniscus is at the upstream edge of the optical fibers
- **Wide end (e_w)**: point 10, last peak in the waveform: the backward meniscus is at the downstream edge of the optical fibers

At this point the droplet temporal size can be defined as the average between the size seen from the left optical fiber edge and the right optical fiber edge: $size = (e_n - s_w + e_w - s_n)/2$. The details on how the edges are extracted from the waveforms are in 4.1.5.

4.1.2 Re-sampling of the signals

After computing the differences in time between two consecutive measures of the photocells system, we noticed that the rate of the acquisitions is not constant, despite we set a constant value for the time interval between successive measurements on the Arduino software ($dt = 10\text{ ms}$). Instead, the actual acquisition rate increases of one millisecond every time the elapsed time reaches a new power of 10, as reported in figure 15. This can be explained considering that the communication between Arduino and the LabView software happens via the serial port, and it takes a certain amount of time (that we assumed negligible, but actually it's not) to print a single character: since the timestamps are printed as the integer number of milliseconds elapsed from the start of the measurement, every time the elapsed time reaches a new power of 10 there is an additional digit to print to the serial port, and so dt rises.

More quantitatively the voltage readings from the two photodiodes are printed as 'A0XXX' and 'A1XXX' where 'XXX' is the digitized voltage (from 0 to 1024 (corresponding to 5 V)), and, since the voltage is almost always between 1 V and 4 V, it consists of three digits. The timestamp is printed as 'TTX...X' having $2 + \text{int}(\log_{10} t|_{[\text{ms}]})$ digits. From figure 15 we can see that when the time is between 1 and 10 seconds $dt = 23\text{ ms}$, 10 of which are the manual delay we set, while the remaining 13 are used to print $5 + 5 + (2 + 4) = 16$ characters to the serial port, confirming the fact that, since the baud rate of the serial port is 9600 bits per second and single characters are 8 bits long, it takes 0.83 ms to print every character.

In order to have a more regular signal (which is important for the next steps of the analysis) we re-sampled every $dt = 10\text{ ms}$ the linear spline of the original signal (see figure 15).

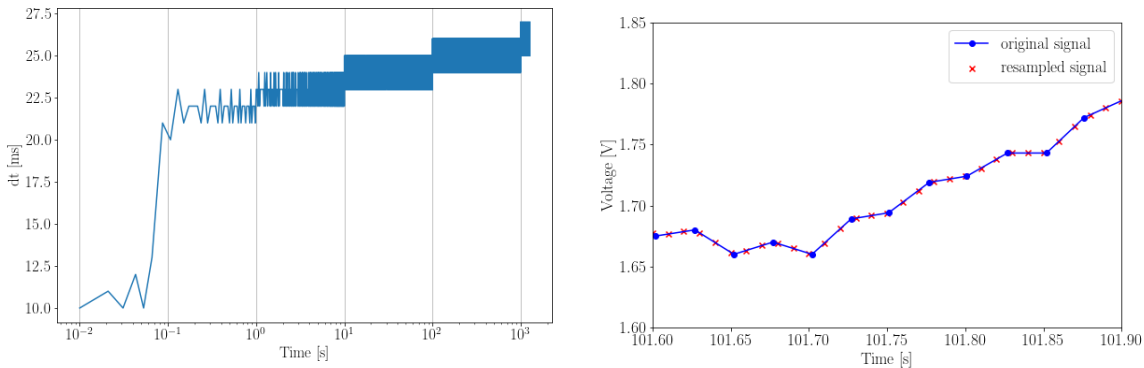


Figure 15: Behavior of the original dt throughout the measurement and example of how resampling works.

4.1.3 Fast Fourier Transform filter

After the re-sampling, the signal is Fourier transformed and filtered in frequency as reported on the left of figure 16, removing the zero frequency component (to have a zero-meaned signal) and the components with frequency above a certain cutoff, in order to reduce the electronic noise. After this frequency cropping, the signal is then anti-transformed. An example of the signal before and after the filtering is reported on the right of figure 16.

4.1.4 Straightening of the signals

Trying to remove the long-period oscillations of the baseline with the Fourier filter method would heavily distort the waveforms, so we decided to straighten the signal in another way, as shown in figure 18. This will prove to be very useful for both thresholds searching and droplet edges identification, as described in next section (4.1.5).

The straightening procedure is the following: at first the mean voltage value, \bar{V} , of the signal is computed, then two thresholds, \bar{V}_{up} and \bar{V}_{down} , are defined as the average of the values above and below \bar{V} respectively. The mean value of the two thresholds is then computed as $\bar{V}_{pivot} = \frac{\bar{V}_{up} + \bar{V}_{down}}{2}$. This allows to correctly identify

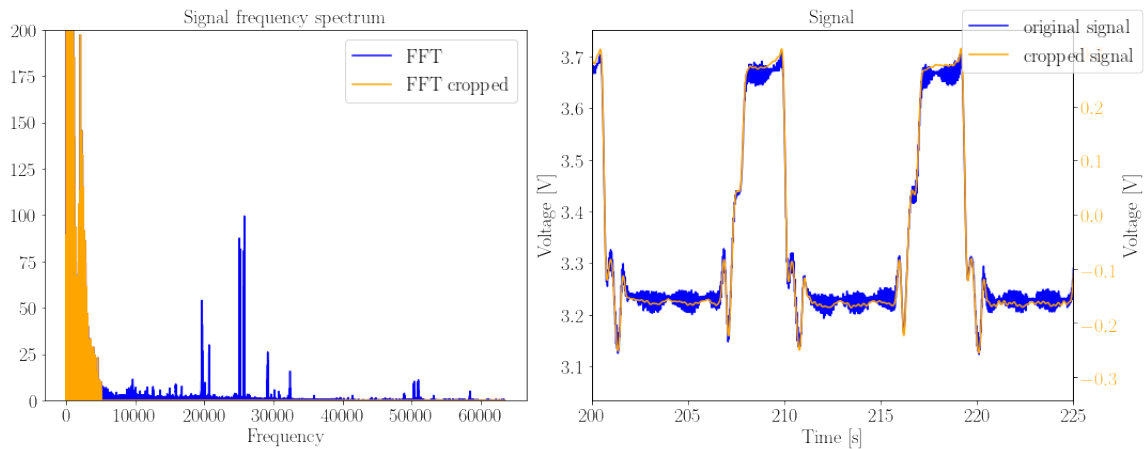


Figure 16: Example of the FFT spectrum (left) and the signal before and after the frequency filtering (right). Acquisition with $q_w = q_o = 2 \mu\text{L}/\text{min}$ (chip B).

the voltage value in the center between the water and oil levels, as \bar{V} would be biased in case the two fluxes are not equal.

\bar{V}_{pivot} is then used to divide the signal in two sections: the *upper* part, where the voltage values are $V(t) > \bar{V}_{pivot} + V_{Bias}$ and the *lower* part, where the signal remains in the range $V(t) \in [V_{thr}, \bar{V}_{pivot} - V_{Bias}]$. The parameter V_{bias} is used to exclude the central data from the baseline identification. V_{thr} is used in order to ignore data below a certain voltage threshold: this allows us to identify the real baseline without considering spikes going downwards due to the effect of the menisci. These parameters are chosen manually for each data-set.

On the left of figure 17 is reported an example of the signal with the thresholds just introduced, while on the right we show the running mean for *upper* and *lower* portions of the signal, which is usually performed using a sliding window of 20 s. They work as fit curves for the baselines.

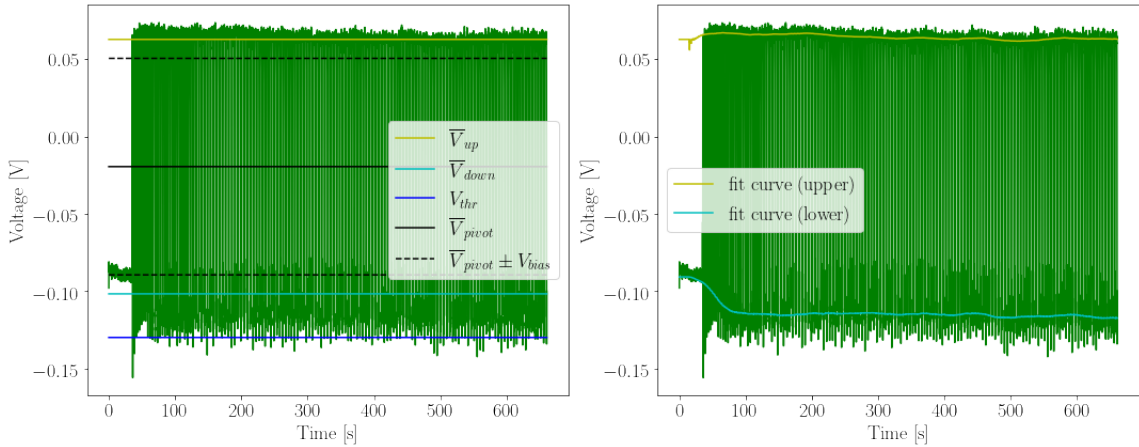


Figure 17: The original signal, with the thresholds used in the rectifying process, on the left and with the two fit curves on the right. Acquisition with $q_w = 3 \mu\text{L}/\text{min}$, $q_o = 7 \mu\text{L}/\text{min}$ (chip B).

With these fit curves, the new signal, $V'(t)$, is created associating the following values:

$$\begin{cases} V(t) \rightarrow V'(t) = V(t) + \bar{V}_{up} - V_{upper}^{fit}(t), & \text{when } V(t) > \bar{V}_{pivot} \\ V(t) \rightarrow V'(t) = V(t) + \bar{V}_{down} - V_{lower}^{fit}(t), & \text{when } V(t) \leq \bar{V}_{pivot} \end{cases} \quad (1)$$

Where $V(t)$ is the original signal.

In order to get a more refined straightening, the procedure is repeated one more time with a smaller window for the running mean (typically 5 s).

An example of an original and the two rectified signals is reported in figure 18. Notice that the amplitude of the signal is not significantly altered during the rectification process. This is particularly important for the correct analysis of the experimental errors as will be described in the section 4.1.6.

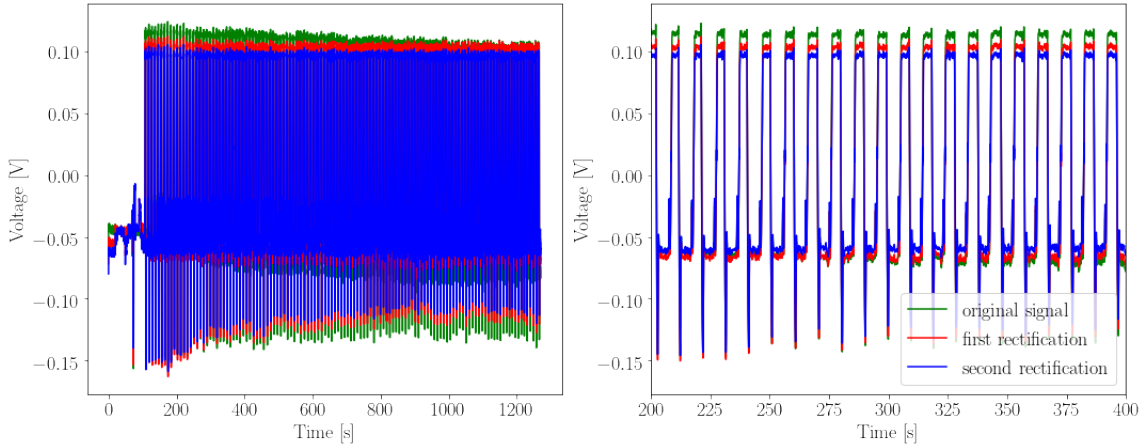


Figure 18: A comparison of the original and the two rectified signals. Acquisition with $q_w = q_o = 2 \mu\text{L}/\text{min}$ (chip B).

4.1.5 Identification of the droplet edges

After manipulating the signals, we were able to face droplet identification with an algorithm that uses two voltage thresholds, which are found fitting the histograms of the signals with two gaussians: the first peak, at lower voltage, corresponds to the oil level, while the second one to the water droplets (see figure 21). We set the thresholds at $V_{low}^{th} = \mu_1 + x_1 * \sigma_1$ and $V_{high}^{th} = \mu_2 - x_2 * \sigma_2$, where μ_i and σ_i , $i = 1, 2$ are the gaussian parameters and x_i values were chosen in order to guarantee the best droplet recognition by the algorithm (anyways $x_i \approx 3$).

Recalling what said in the study on the shape of the waveforms (section 4.1.1), we can operationally define how to compute the four droplet edges: the narrow start s_n corresponds to the first time the signal overcomes V_{high}^{th} after being below V_{low}^{th} , while the narrow end e_n is the last time the signal was above V_{high}^{th} before going below V_{low}^{th} . The wide edges s_w and e_w are instead defined as where the voltage value has a maximum between the second and third crossing points (red circles in figure 19) with V_{low}^{th} respectively before s_n and after e_n .

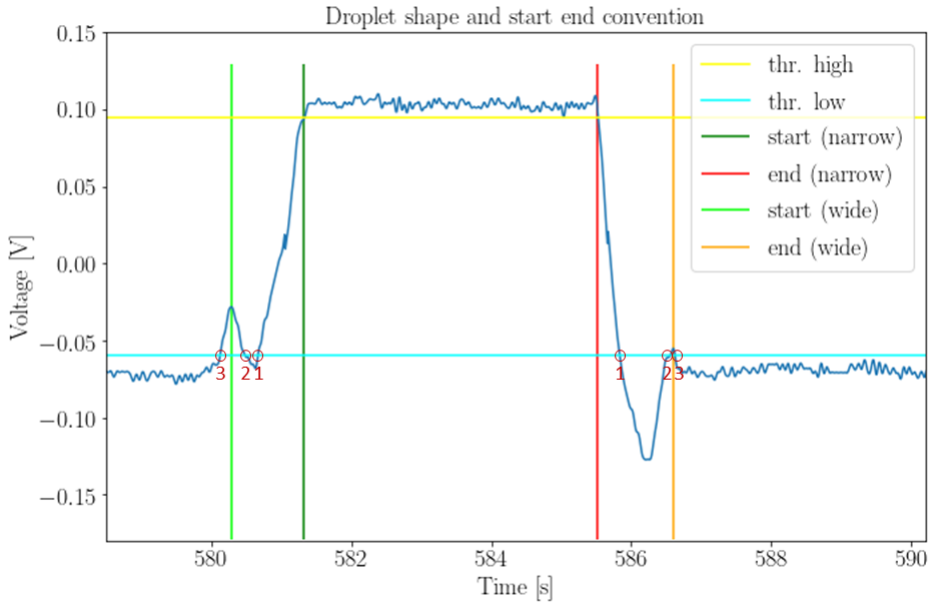


Figure 19: Identification of the droplet edges

Missed droplets checking Sometimes the peak corresponding to the drop **wide end** can be too small to be identified, i.e. it does not cross the **low threshold**. In these cases the algorithm misses the correct **wide end** instant, and instead it detects the first peak above the **low threshold** which is the **wide start** of the following droplet (see figure 20). We cannot simply set a lower **threshold** since it would be, for some droplets, at a lower voltage than the minimum of the signal between s_w and s_n (it's the case of the first droplet in figure 20). So, instead, the software checks if the instants of a **wide end** and the following **wide start** are equal and, in these cases, the correct **wide end** of the droplet is taken as the first local maximum after crossing the **low threshold** after e_n , which is found computing the signal derivative.

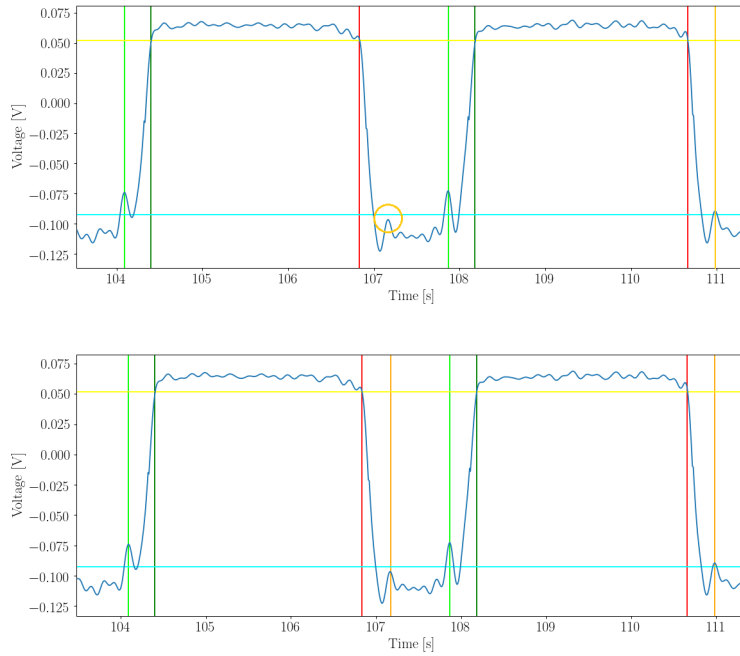


Figure 20: On the top, the wide end of the first droplet is confused with the wide start of the second droplet while, on the bottom, the peak is correctly identified. Acquisition with $q_w = 7 \mu\text{L}/\text{min}$, $q_o = 3 \mu\text{L}/\text{min}$ (chip B).

The role of signal straightening can be appreciated by looking at figure 21, where the low voltage peak in the histogram was bimodal due to the variation of the height of the oil baseline during data collection. This made impossible to detect the small menisci spikes in all the droplets by using constant value thresholds. Instead, with straightened data there is a single peak corresponding to the fluctuations due to the menisci, which allows to properly find all the droplet edges.

One should notice that with this definition the wide edges are independent from the actual value of the lower threshold, while the narrow ones depend on V_{high}^{th} . For this reason, for consistency throughout different datasets, we fixed $x_2 = 3$ when defining the thresholds.

4.1.6 Errors of measurement

The measures acquired with the photocells system are subjected to an uncertainty on the voltage values, due to the digitization of the signal performed by the Arduino board's Analog to Digital Converter, and to an uncertainty in the time, due to the finite rate of acquisition.

Voltage errors As described in section 2, the voltage precision of the electric signals is $\Delta V = 4.88 \text{ mV}$. Assuming a uniform distribution of the values between each channel, the experimental error on the voltage measurements is $\sigma_V^{res} = \frac{\Delta V}{\sqrt{12}} = 1.4 \text{ mV}$. Since the straightening process does not alter the amplitude of the signal, this error does not change after signal processing.

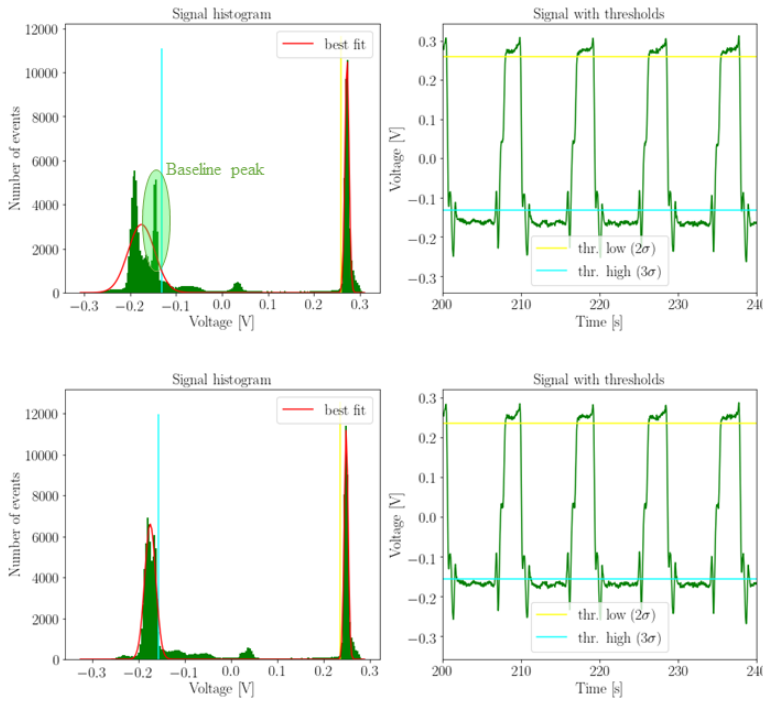


Figure 21: Thresholds searched for the Fourier filtered signal without rectification (on the top) and with the signal rectified (on the bottom). Acquisition with $q_w = q_o = 2 \mu\text{L}/\text{min}$ (chip B).

Time errors Similarly we can associate to the time measurement t an error $\sigma_{res}(t) = \frac{\Delta t(t)}{\sqrt{12}}$ where $\Delta t(t)$ is the time interval between two consecutive measurements at time t in the non resampled signal (which, as we have seen from section 4.1.2 is not constant over the acquisition).

While the error on the wide edges is simply σ_{res} , a further term must be considered for the narrow ones: the water baseline has a voltage oscillation that can be estimated as the sigma parameter σ_V^{high} of the gaussian fit of the voltage histogram (section 4.1.5). This voltage oscillation affects the narrow start and narrow end identification, so it must be translated into a temporal uncertainty. Since the two narrow edges are defined as the instant (s_n and e_n) when the voltage crosses the high threshold, we considered the error over these instants equal to the projection of the voltage error on the time axis. To determine it, we computed the slope of the signal around the threshold, and assumed $\sigma_V = slope * \sigma_t$. In figure 22 it is reported an example of the two slopes just described.

Since $\sigma_V^{high} \gg \sigma_V^{res}$ we can neglect the latter in the projection, and so the final time errors for the drop edges are then:

$$\sigma(s_n) = \sqrt{\sigma_{res}(s_n)^2 + \left(\frac{\sigma_V^{high}}{slope(s_n)} \right)^2} \quad \sigma(s_w) = \sigma_{res}(s_w) \quad (2)$$

And similarly for e_n and e_w ; $slope(t)$ is the local slope of the signal at time t , computed with a linear fit of a few points around time t .

All the errors on the following derived quantities are determined by propagation.

4.1.7 Droplet characterization

After detecting the drop edges in the electronic signal we calculated the time duration of the droplet signal (temporal size) for each photo-detector as explained at the end of 4.1.1. Similarly, we computed the temporal distances between subsequent drops and the temporal period of droplet pattern, which is the reciprocal of their

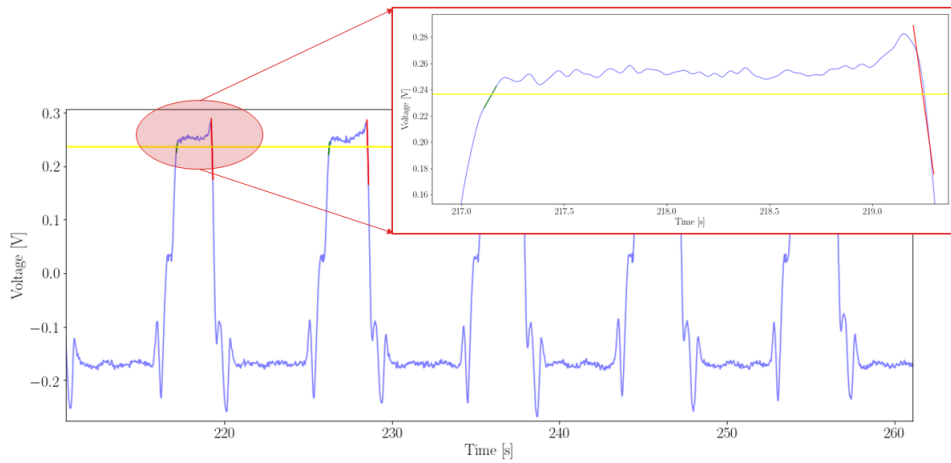


Figure 22: Acquisition with $q_w = q_o = 2 \mu\text{L}/\text{min}$ (chip B).

frequency. So we have for the i^{th} drop:

$$\begin{aligned} size_t^i &= \frac{e_n^i - s_w^i}{2} + \frac{e_w^i - s_n^i}{2} \\ distance_t^i &= \frac{s_w^{i+1} - e_n^i}{2} + \frac{s_n^{i+1} - e_w^i}{2} \\ period_t^i &= \frac{s_w^{i+1} - s_w^i}{4} + \frac{s_n^{i+1} - s_n^i}{4} + \frac{e_n^{i+1} - e_n^i}{4} + \frac{e_w^{i+1} - e_w^i}{4} \end{aligned}$$

Being able to recognize the corresponding droplet in signal 1 and signal 2, we computed the time interval that it takes for every single droplet to transit from detector 1 to detector 2. Knowing the nominal¹ spatial distance between detectors (50 mm), we computed also the velocity v of the droplets as a function of time. Multiplying the temporal size or distance and the velocity droplet by droplet, we finally obtained sizes and distances in terms of space: $size_s^i$ and $distance_s^i$.

We also realized that an estimation of the optical fiber size could be obtained considering the difference between s_n and s_w or the difference between e_w and e_n , coherently with the meaning of the waveforms in 4.1.1:

$$fiber_s = \left(\frac{s_n - s_w}{2} + \frac{e_w - e_n}{2} \right) v \quad (3)$$

In figure 23 we can see the trends of these quantities as a function of the drop index for both signal 1 and signal 2. On the right of each graph we plot their corresponding Extended Kernel Density Estimate (EKDE), which is obtained with the point-wise sum, running on the different droplets, of Gaussian functions with area 1 and mean and standard deviation of the specific measure they resemble. In formulas, if there are N droplets each with a particular property \mathcal{P} with value p and standard deviation $\sigma(p)$,

$$EKDE(x) = \sum_{i=1}^N \mathcal{G}(x; 1, p_i, \sigma(p_i)) \quad \mathcal{G}(x; A, \mu, \sigma) = \frac{A}{\sqrt{2\pi}\sigma} e^{-\frac{(x-\mu)^2}{2\sigma^2}}$$

So now $EKDE(x)$ is the probability density function for the property \mathcal{P} and can be fitted with a Gaussian (see figure 23). The results of the fits are reported in table 1.

For the majority of the quantities we calculated, we observe that they reach a stationary regime some minutes after switching on the water flux ($t = 0$ s). We needed to start the acquisition before reaching a steady state, in order to be able to identify the corresponding droplet signal in the two photocells, as explained in section 3. We also noticed that the velocity did not reach a constant value, even after 20 minutes of data-taking for the dataset shown in figure 23. This is true also for some of the other datasets, so we couldn't give a mean value

¹More on that in section 5.

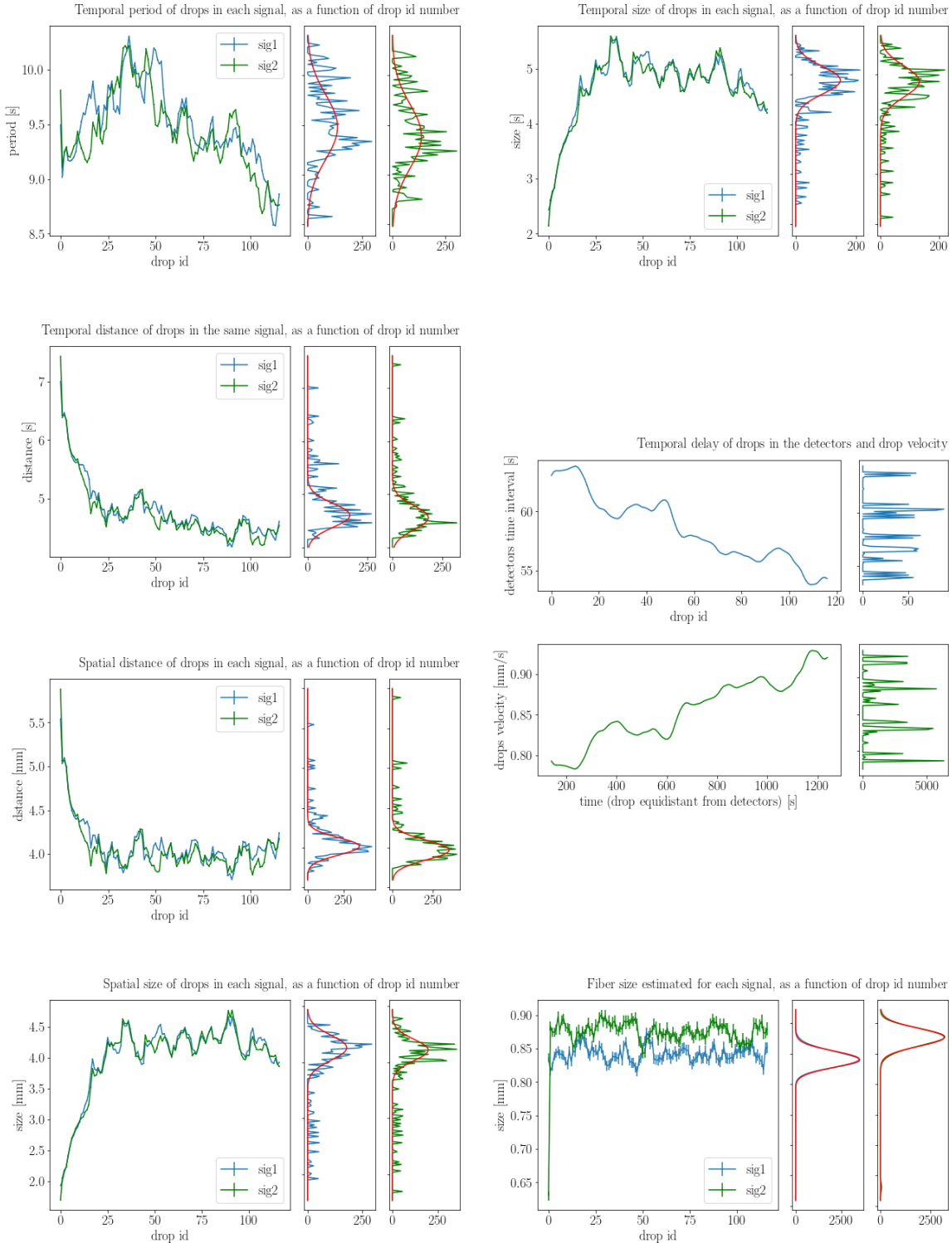


Figure 23: Droplet temporal period, size and distance, time interval and velocity, spatial size and distance, optical fiber spatial size from the electronic analysis on the dataset with $q_o = q_w = 2\mu L/min$

Property	mean	standard deviation
temporal size [s]	4.87 ± 0.01	0.3 ± 0.1
temporal distance [s]	4.580 ± 0.009	0.224 ± 0.009
temporal period [s]	9.43 ± 0.02	0.32 ± 0.02
spatial size [mm]	4.237 ± 0.009	0.20 ± 0.04
spatial distance [mm]	3.994 ± 0.003	0.081 ± 0.009
fiber 1 size [mm]	0.84092 ± 0.00005	0.01334 ± 0.00005
fiber 2 size [mm]	0.87692 ± 0.00005	0.01459 ± 0.00005
dt [s]	57.5 ± 0.2	
velocity [mm/s]	0.870 ± 0.003	

Table 1: Results of the fits for the dataset with $q_o = 2 \mu\text{L}/\text{min}$, $q_w = 2 \mu\text{L}/\text{min}$. Velocity and time interval between detectors are not obtained directly fitting the data.

for the velocity estimation by fitting the EKDE. Instead, we estimated it as the ratio between the mean values of the spatial size and of the temporal size of the drops and reported it in table 1. We used this values for some comparisons between the dataset (see section 5).

In general there is a good agreement between the quantities measured with the two different detectors. The only exception is for the optical fiber size. Its real value would be 1 mm, but the value that can be deduced from the droplet waveform depends on the alignment of the two optical fibers in the joint; in particular it corresponds to the length of the superposition of their projections. So we expect to measure values equal or smaller (due to a slight misalignment between the fibers) than 1 mm. Of course signal 1 and signal 2 correspond to two different joints, so we expect the fiber size values to be different.

4.2 Videos

4.2.1 Image preprocessing

For each video, the first thing to do is extracting the frames, which are arrays of 960×1280 RGB pixels, selecting only the green channel (the one with the higher contrast since droplets are pink-reddish) and converting it to a gray scale.

At this point we computed the mean of all the frames and subtracted it to every frame, eventually rescaling the values of the pixels to avoid underflow or overflow, which allows us to remove all stationary features such as lighting gradient or the ruler. One should notice that in order to be able to compare different images of the same video, this rescaling procedure and whatever else transformation that is applied to the images must be applied in the same way to all the images of the video.

After the mean subtraction we took the negative of the images to have the water droplets brighter than the oil: this is just for consistency with the electronic signals where the droplets produced a higher voltage.

Since to maximize the length of capillary observed in the video, it was oriented to be along the diagonal of the images, we now rotate them (adding extra black pixels around it not lose the corners of the image) to make the capillary as horizontal as possible.

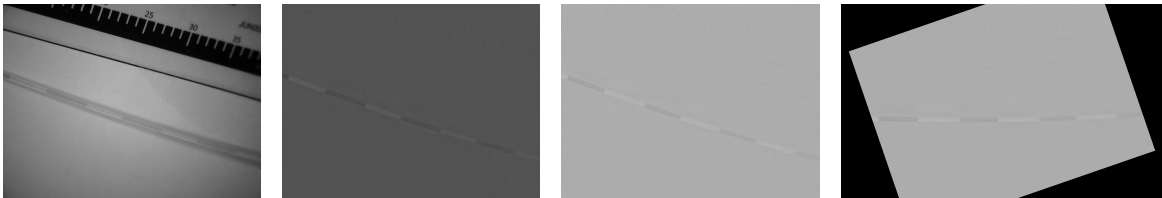


Figure 24: Preprocessing steps performed on a sample image: from left to right conversion to gray scale, mean subtraction, negative, rotation.

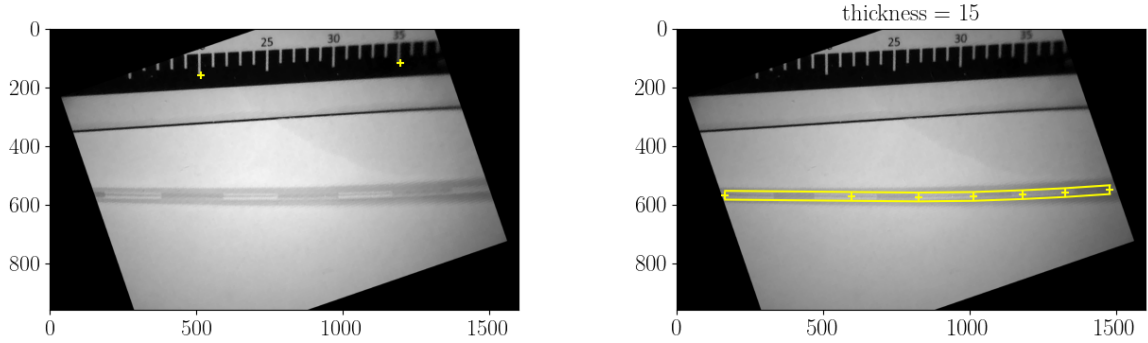


Figure 25: Calibration of the images using the ruler and highlight of the capillary region.

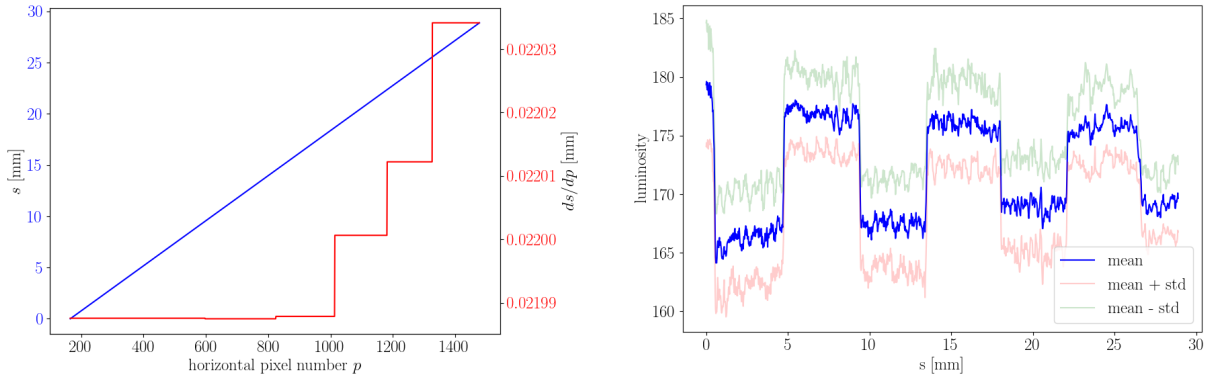


Figure 26: On the left s coordinate (blue) and its derivative (red) both plotted against pixel number. On the right luminosity waveform extracted from the image.

4.2.2 Waveform extraction

At this point we chose an image from the original video, with only the rotation applied, and used it for calibration (i.e. converting distances from pixels to mm) and to find the position of the capillary (figure 25). For the latter we manually set some points on the center of the capillary and then connect them with line segments. Such linear spline allows us to put a coordinate s (in mm for the position along the capillary of each pixel, that accounts for the slope of each segment (see figure 26 (left)). Then for each pixel on the spline we select a vertical line of $2h+1$ pixels centered on that particular pixel and compute mean and standard deviation of the luminosity. What we obtain is then associated to the s coordinate of that pixel, resulting in a waveform (see figure 26 (right)). For the example here shown, we used $h = 15$.

4.2.3 Finding the droplets edges

Now that we obtained a waveform from every image, we can apply, with some tweaks, the same techniques used on the electronic signals. First of all since the difference in luminosity between oil and water is well distinguishable with respect to the standard deviation of the waveform, we can directly use just the mean. Second, as can be seen in figure 26 there is a trend in the amplitude of the oscillation and since here the signal has too few points to successfully use the FFT, we directly proceed with rectification similarly to what has been done for the electronic signals. In particular we used just one iteration and a window for the running average of 5 mm.

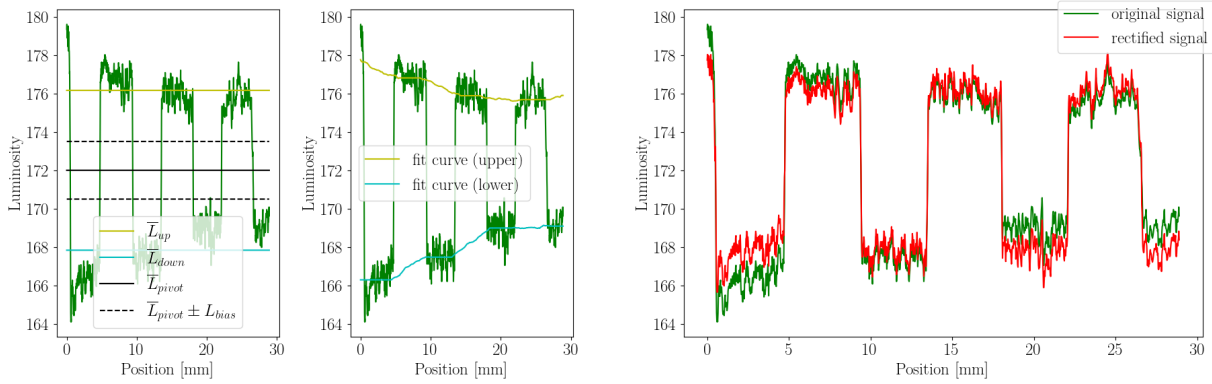


Figure 27: Rectification of the waveform and comparison between original and rectified signal.

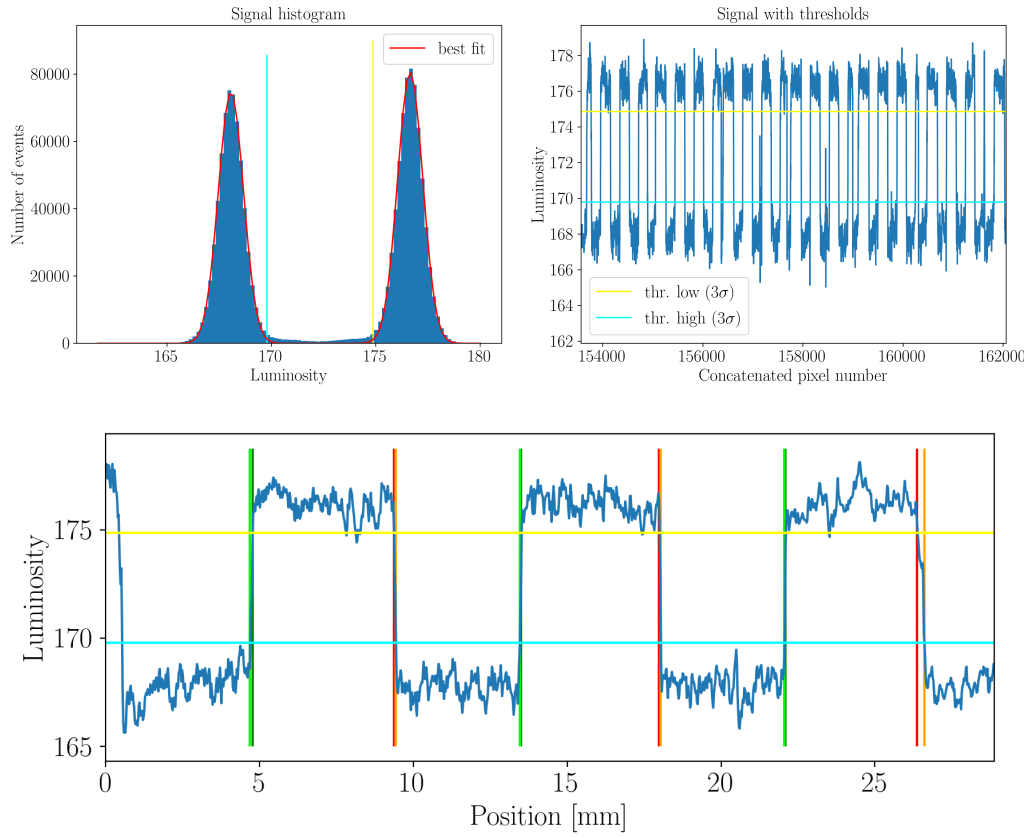


Figure 28: Histogram of the luminosity for finding the thresholds and their position in a sample portion of the data (top) and identification of the droplets edges (bottom)

Then for the horizontal thresholds we concatenated all the rectified waveforms from every frame of the video to compute a more meaningful histogram of the luminosity. With these thresholds we then identified the edges of every drop (see figure 28).

Since in the signals from the videos we directly see the droplets, the waveform is much more simple and easier to interpret with respect to the electronic signals, thus we defined the narrow start and end in the same way as for the electronic signals; however the wide start and end are respectively defined as the last time the signal was below the lower threshold before the narrow start and the first time it goes below it after the narrow end. The narrow size (*narrow end - narrow start*) will be the size of the droplets without the menisci, while *narrow start - wide start* and *wide end - narrow end* will be the sizes respectively of the backward and forward menisci.

One has to notice that with this definition all droplet edges are dependent on the values of the thresholds,

and so, for consistency, we set the thresholds at 3σ from their peak for every dataset. Also, since all edges are at a point where the signal crosses a threshold, they all have an error contribution both from the resolution (width of the pixels) and from the projected error of the luminosity, as was done for the narrow edges in the electronic signal.

4.2.4 Identifying the droplets

At this point if one plots size and distance between the droplets against the frame id, one would get the plot in figure 29 (left), which shows a clear trend in the first frames, symptom of the fact that to correctly identify the droplets in the electronic signal we started the acquisition just after turning on the water pump, thus far from being in stationary conditions. Nevertheless, this transient seems to occupy a quite small portion of the data.

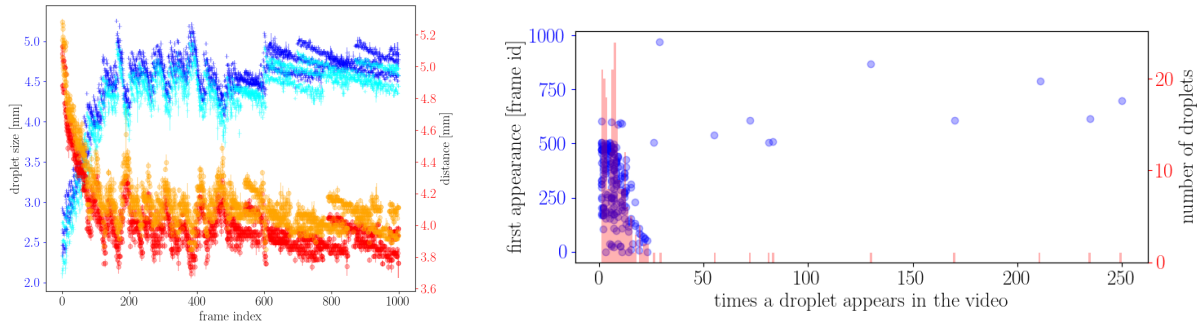


Figure 29: Plot of the size and distance between droplets (left) for the dataset on chip B with $q_o = q_w = 2 \mu\text{L}/\text{min}$. Wide and narrow size respectively in blue and cyan and wide and narrow distance respectively in red and orange. Histogram of the recurrence of each Droplet compared with their first appearance in the video (right)

Even if this plot is useful for getting a fast and rough analysis of the data, it cannot be used to compute statistics on the droplets, since every physical droplet appears many times in the video and should be counted just once. So, to correctly identify the droplets we then assigned an id to every droplet in every frame and compared consecutive frames such as if two appearances of a droplet had a quite similar size and the difference in position was compatible with the expected velocity computed from the oil and water fluxes, the two appearances were considered to belong to the same droplet and so they will share the same id. At the end of this process we have a list of 'Droplet' objects resembling the physical droplets and containing every appearance of that particular droplet (henceforth when we write Droplets with the capital letter we refer to these objects).

However, as we said before, due to issues in the microscope timelapse program, frames aren't shot precisely every spf seconds, and thus the computed velocity is pretty chaotic. For example for $q_o = q_w = 2 \mu\text{L}/\text{min}$ the expected velocity is 0.943 mm/s, but the computed velocity spans from 0 up to 5 mm/s (third plot in figure 31). Our hypothesis is that the timelapse program works by storing images in a buffer and once it needs to empty it, it takes some time during which it cannot take more pictures, thus producing a 'jump', namely a peak in the computed velocity (see figure 30). Doing so it accumulates some delay with its internal schedule for taking pictures, and so, to compensate, in the last part of the video it shoots them far more frequently than it should, resulting in a much lower computed velocity (we even experienced two consecutive frames to be exactly the same picture). The symptom of this is that the last Droplets in the video appear far more times than the others, namely they have a much higher 'recurrence' (see figure 29 right).

4.2.5 Droplet statistics

Now that we have a list of Droplets we can proceed in computing statistics. First of all there are two choices for the error of each property of every Droplet: the error of the mean computed with the error propagation on the formula of the arithmetic mean or the error of the mean as the standard deviation of all the different

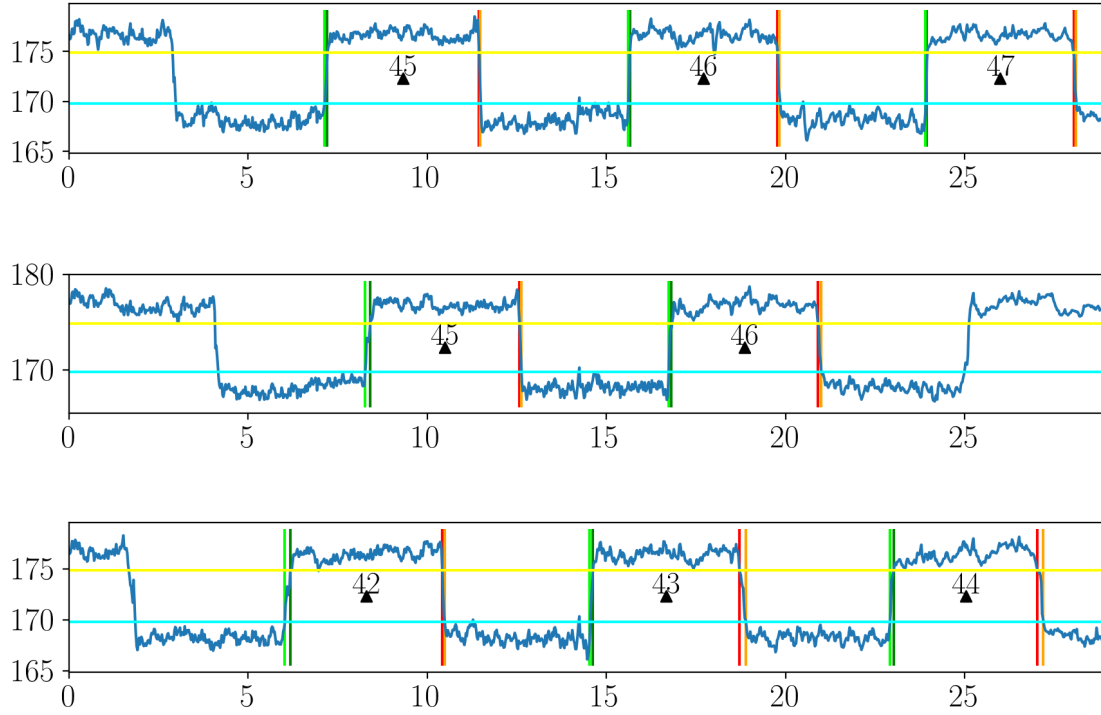


Figure 30: Position of the droplets in frames 469, 470, 471. Between the last two frames there is a jump so high that the algorithm fails to correctly identify the droplets: Droplets 43 and 44 were actually 45 and 46.

appearances divided by the square root of the number of appearances. Since these two approaches lead to quite similar results, to be conservative we took, case by case, the maximum between the two.

At this point we can plot how the different properties behave along the video and then produce for every property an Extended Kernel Density Estimate. Similarly to the electronic analysis, we fitted it with a Gaussian (see figure 31). The results of the fits are in table 2.

Property	mean	standard deviation
distance wide [mm]	3.982 ± 0.004	0.101 ± 0.004
distance narrow [mm]	4.126 ± 0.003	0.103 ± 0.003
wavelength [mm]	8.553 ± 0.005	0.143 ± 0.005
size wide [mm]	4.570 ± 0.008	0.218 ± 0.008
size narrow [mm]	4.399 ± 0.007	0.228 ± 0.007
backward meniscus size [mm]	0.0864 ± 0.0004	0.0202 ± 0.0004
forward meniscus size [mm]	0.0759 ± 0.0005	0.0204 ± 0.0005
velocity [mm/s]	1.47 ± 0.03	0.93 ± 0.03

Table 2: Results of the fits for the dataset with $q_o = q_w = 2 \mu\text{L}/\text{min}$.

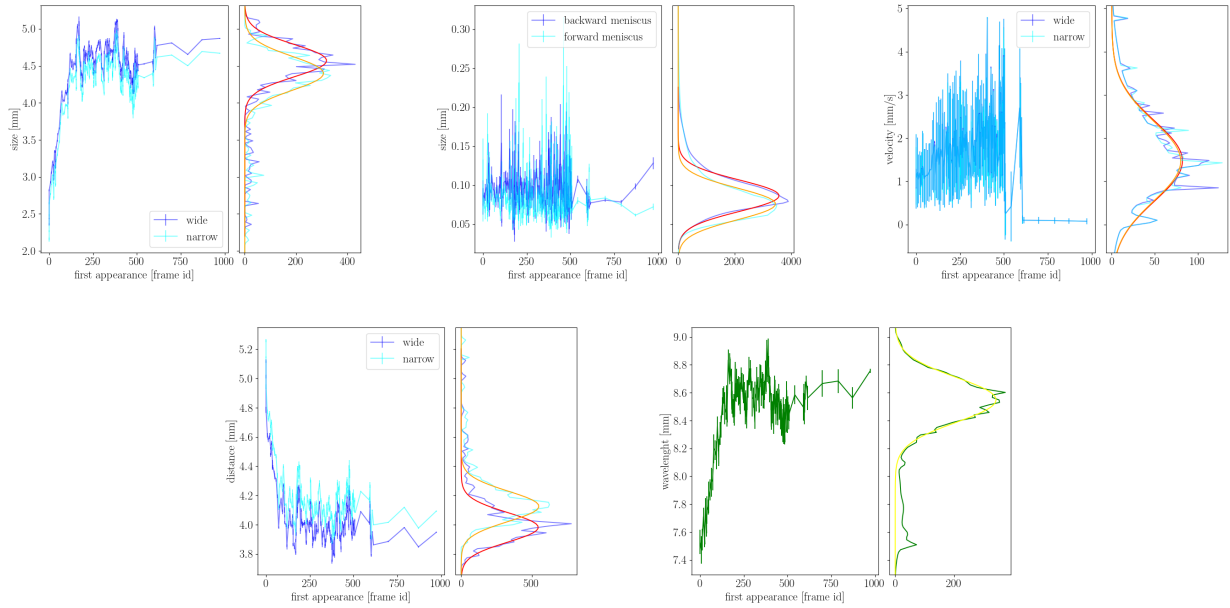


Figure 31: Behavior of the properties of the Droplets along the video and EKDE fits on the side of each plot. The red fit refers to the blue curve and the orange to the cyan one. The first three plots are of size, meniscus size and velocity, which are properties intrinsic to a single droplet. The second two plots, distance (end to start) and wavelength (i.e. distance center to center) use the relation of every Droplet with the next one.

5 Results

In this section we gather the estimates obtained from electronic analysis and image processing, for both Chip B and Chip A. Notice that in the following plots data have been artificially misaligned on the x axis to better see the error bars: when this is done a vertical dotted gray line represents the true x coordinate of the data points close to it.

Issues with chip A Concerning electronic analysis, the size of the droplets produced by chip A is similar to the fiber size or even smaller. This means that light from the optical fibers hardly ever passes through only water, thus in the waveforms there is no plateau corresponding to the water baseline and so we cannot properly apply our algorithm for the waveform interpretation and it is thus difficult to find the droplet edges. Furthermore considering that the actual time interval between electronic measurements is around 22 ms instead of the 10 ms we assumed when planning at which fluxes take the data, we ended up with too fast droplets and thus a too low resolution in the waveforms which made impossible to extract meaningful information from most datasets of chip A. We should have collected datasets with smaller fluxes, but since developing a method for signal analysis took quite long, we didn't realize this problem before taking down the experimental setup.

So at the end of the day we managed to successfully analyze the electronic signal only of the slowest dataset ($q_o = q_w = 0.5 \mu\text{L}/\text{min}$). On the other hand we were able to successfully analyze the videos of a couple more datasets.

Comparison between electronic and image analysis In table 3 we show a comparison between droplet size, distance velocity and wavelength obtained from the analysis of electronic and image data. The error on the quantities reported is the standard deviation of the gaussian fitting the data, thus emphasizing the distribution of the measured quantities along the acquisition. As we can see, the electronic analysis underestimates all spatial properties², and this is most likely due to an underestimation of the velocity that we used for converting temporal quantities to spatial ones. More on that later.

²The ones extracted from the image analysis are much simpler to compute (we directly measure the droplets) so they are more reliable.

$q_o, q_w (\mu\text{L}/\text{min})$	Property	electronic	microscope (narrow)	microscope (wide)
$q_o = 2, q_w = 2$	size [mm]	4.2 ± 0.1	4.4 ± 0.2	4.6 ± 0.2
	distance [mm]	4.00 ± 0.08	4.1 ± 0.1	4.0 ± 0.1
	velocity [mm/s]	0.87 ± 0.03	1.5 ± 0.9	1.5 ± 0.9
	wavelength [mm]	8.2 ± 0.2	8.5 ± 0.1	
$q_o = 5, q_w = 5$	size [mm]	4.00 ± 0.09	4.3 ± 0.2	4.4 ± 0.2
	distance [mm]	3.72 ± 0.06	3.9 ± 0.1	3.8 ± 0.1
	velocity [mm/s]	2.20 ± 0.09	3 ± 2	2.2 ± 0.1
	wavelength [mm]	7.7 ± 0.1	8.1 ± 0.1	
$q_o = 3, q_w = 7$	size [mm]	7.3 ± 0.3	7.6 ± 0.5	7.8 ± 0.5
	distance [mm]	2.93 ± 0.06	3.02 ± 0.08	2.92 ± 0.08
	velocity [mm/s]	2.25 ± 0.08	3 ± 2	3 ± 2
	wavelength [mm]	10.3 ± 0.3	10.6 ± 0.3	
$q_o = 7, q_w = 3$	size [mm]	2.55 ± 0.07	2.7 ± 0.1	2.8 ± 0.1
	distance [mm]	5.0 ± 0.1	5.2 ± 0.2	5.1 ± 0.1
	velocity [mm/s]	2.30 ± 0.05	3 ± 2	3 ± 2
	wavelength [mm]	7.6 ± 0.1	7.9 ± 0.1	
$q_o = 10, q_w = 10$	size [mm]	4.03 ± 0.09	4.2 ± 0.1	4.4 ± 0.1
	distance [mm]	3.44 ± 0.05	3.63 ± 0.05	3.52 ± 0.05
	velocity [mm/s]	4.1 ± 0.1	3 ± 2	3 ± 2
	wavelength [mm]	6.5 ± 0.1	7.9 ± 0.1	
$q_o = 15, q_w = 5$	size [mm]	1.92 ± 0.06	2.1 ± 0.1	2.2 ± 0.1
	distance [mm]	5.3 ± 0.1	5.5 ± 0.2	5.3 ± 0.2
	velocity [mm/s]	4.47 ± 0.08	3 ± 2	3 ± 2
	wavelength [mm]	7.3 ± 0.1	7.6 ± 0.1	
$q_o = 5, q_w = 15$	size [mm]	8.8 ± 0.2	9.2 ± 0.3	9.3 ± 0.3
	distance [mm]	2.68 ± 0.09	2.83 ± 0.03	2.71 ± 0.03
	velocity [mm/s]	4.7 ± 0.1	4 ± 3	4 ± 3
	wavelength [mm]	11.5 ± 0.2	11.9 ± 0.4	

Table 3: Comparison between droplet size, distance, velocity and wavelength estimations obtained from the electronic data and from the image data (wide and narrow) for chip B at different fluxes.

Frequency and wavelength On the right of figure 32 we can see the estimated wavelength of the droplets, i.e. the spatial period characterizing the droplet train. We observe that this wavelength depends on the geometrical properties of the junction (chip A has smaller droplets more close to each other than chip B), but it is not very sensitive with respect to the total flux. For chip B we also notice that two points, ($q_o = 3, q_w = 7$) and ($q_o = 5, q_w = 15$), seem not to follow the linear trend of the remaining datasets: we may hypothesize the presence of two regimes, but the data is certainly not sufficient to state this.

Also here we can better see the underestimation of the wavelength by the electronic analysis. More quantitatively on average the electronic wavelength is 0.94 ± 0.01 times the one computed from image analysis.

Since the wavelength is about constant with respect to the total flux, we expect the frequency to depend linearly on the total flux, with zero intercept. So we performed a linear fit (the parameters are reported in the graph) and we can see that the intercept q is actually compatible with 0 and so we can write

$$f|_{[\text{Hz}]} = (0.029 \pm 0.003)q|_{[\mu\text{L}/\text{min}]}$$

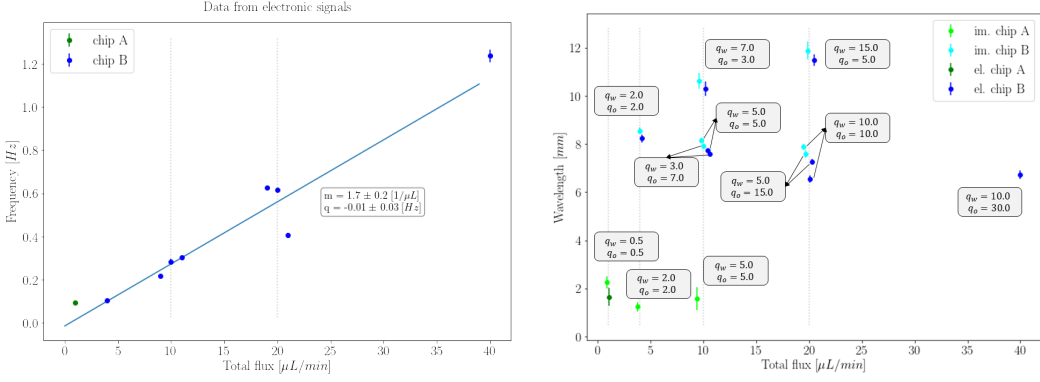


Figure 32: On the left frequency from electronic signal, on the right wavelength for both images (light green for chip-A, light blue for chip-B) and electronics (dark green for A and dark blue for B) as a function of the total flux

Size and distance ratio vs flux ratio On the left of figure 33 we plotted the ratio between the droplet mean distance and the mean wavelength versus the ratio between oil flux and the total flux. On the right there is the ratio size-wavelength versus the ratio water and total flux. Because of volume conservation we expect this data to sit on a straight line with intercept zero and slope one. The intercept is compatible with zero in both cases, however for the distance and the size plot, the slope is respectively 0.94527 ± 0.00003 and 1.0492 ± 0.0001 . This displacement from one can be partially explained with the droplet shape, which is not perfectly cylindrical because of the presence of menisci, making the size of the droplets not linearly proportional to their volume. However the most probable explanation is that our method of choosing where to put the drop edges slightly overestimates the size of the droplets and thus underestimates the distance.

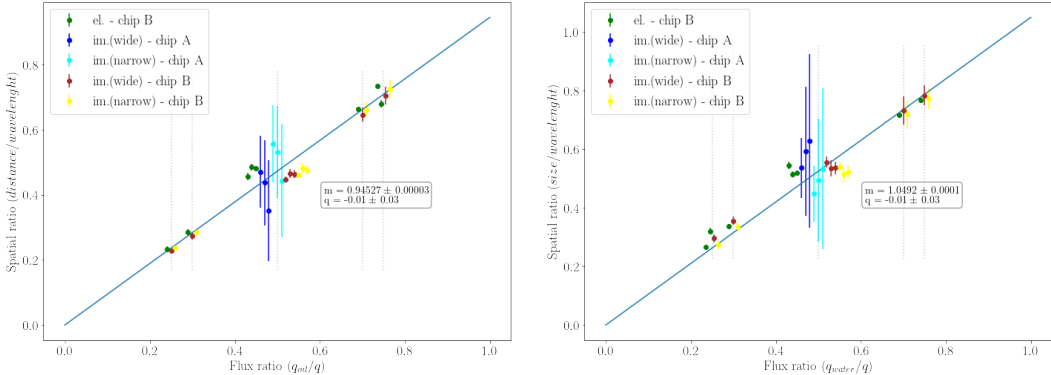


Figure 33: Spatial ratio as function of the oil flux fraction (on the left) and the water flux fraction (on the right)

Velocities In the right plot in figure 34 we show the droplet velocity as a function of the total flux for electronic and image analysis in chip B. According to the calculation in section 3 we expect the slope to be $m = 0.236 \text{ mm min}/\mu\text{Ls}$. Instead we obtained $m = 0.22040 \pm 0.00001 \text{ mm min}/\mu\text{Ls}$, proving that there is a substantial underestimation of the droplet velocity. On the other hand if we compute the velocity as the wavelength extracted from the image analysis times the frequency from the electronic analysis, we obtain the right plot of figure 34 which, once fitted, yields $m = 0.237619 \pm 0.000007 \text{ mm min}/\mu\text{Ls}$ which is far closer to the expected value.

This second estimate of the velocity is more reliable since derives from more simple measurements in both analysis methods, namely a spatial measurement on the image analysis which doesn't need to consider the correlations between different frames, and a temporal measurement on the electronic signals that doesn't need to consider correlations between the two photocells.

At this point both velocity estimates from the two methods alone are incorrect. The one from the image analysis relied on the hypothesis of frames being taken at a constant rate, hypothesis which is heavily violated (see 4.2.4), explaining why we have huge errors on this velocity estimate. On the other hand there are two

possible sources of error in the estimate of the velocity from the electronic signals:

- The distance between the detectors is more than 50 mm: this can be partially explained considering that the distance between the two detectors *along the capillary* may be higher than the free space distance between them if the capillary has somewhat of a curve. However with our setup (figure 5) the capillary is pretty straight, so this effect could add at most 1 mm to the free space distance, and to fully explain our discrepancy in velocities we would need an effective separation of 53 mm.
- We misidentified the droplets appearances in the two detectors. However this is very unlikely since we explicitly started the acquisition before the droplet train reached the detectors. Another source of error could be the fusion of two consecutive droplets between the two detectors which would have caused a misidentification, however this would have also produced a discontinuity in the behavior of the velocity during the acquisition, discontinuity that we did not observe.

With the data we have we are not able to fully explain this perplexing result, for future experiments it will help to have more photocells or even just a better microscope able to take pictures at regular time intervals, which would have allowed us to easily estimate the velocity from the image analysis.

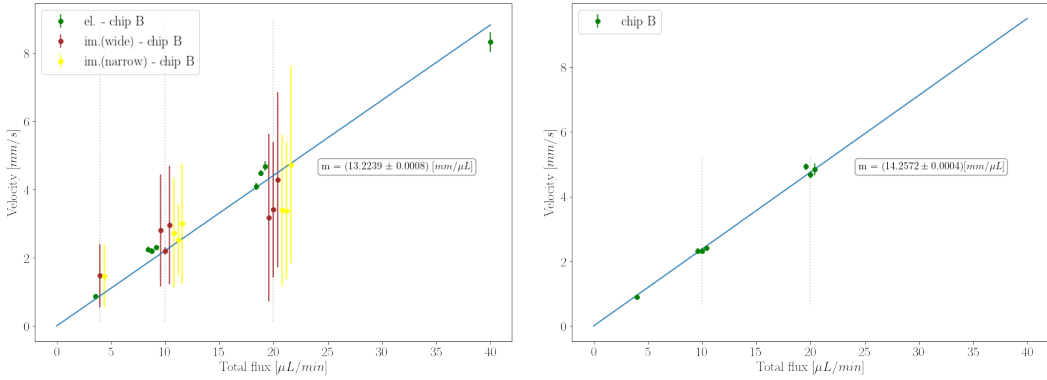


Figure 34: Velocity as function of the total flux, on the left by isolated estimates, while on the right computed as the ratio between the wavelength from image analysis and the temporal period from the electronic one.

Fiber thickness In figure 35 we show the estimated thickness of the optical fibers. The real thickness is 1 mm; smaller values can be explained with an imperfection in the fibers horizontal alignment in the capillary-fiber joint, while values higher than 1 mm have a high uncertainty, and anyway the system can see a greater thickness in case of fiber flattening because of them being slightly squished in the joint.

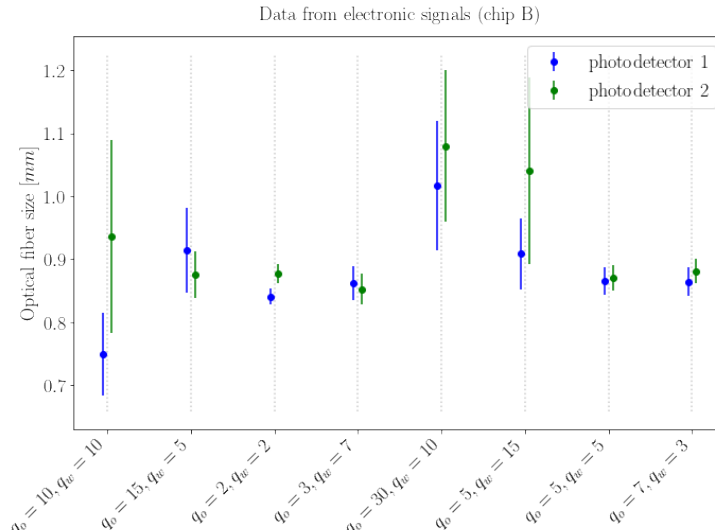


Figure 35: Optical fibers size for each dataset

Menisci size On the left of figure 36 we plot the front and back menisci size, obtained from the image analysis, as a function of the total flux. There is no clear trend in the average size of the menisci, however the difference between the size of the front and back menisci increases with the flux (right plot). In fact, at higher fluxes, the droplet drag with the capillary increases, which means that the front meniscus is elongated, while the backward one is shortened.

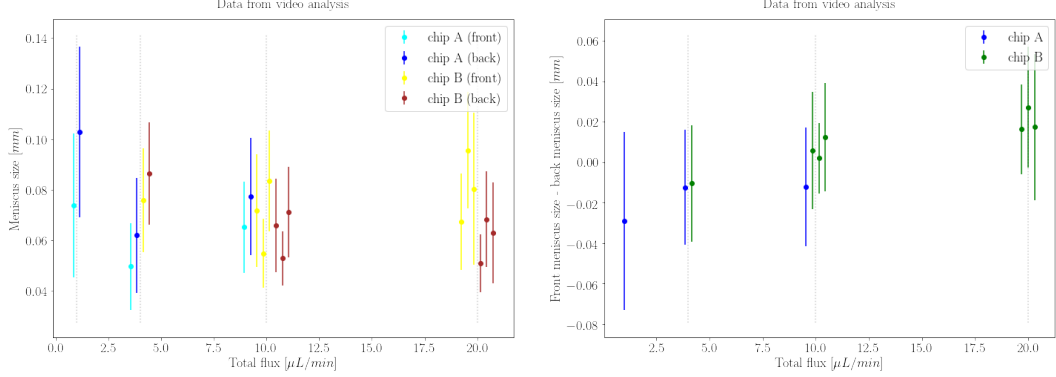


Figure 36: Front and back menisci size as function of the total flux (on the left) and their difference (on the left)

6 Conclusion

Summarizing, we were able to measure the size, distance and menisci size of the droplets at different oil and water fluxes using the image analysis. From the electronic analysis we estimated the frequency of droplet generation and by combining the two approaches we managed to obtain a meaningful estimate of the droplets velocity. We were also able to use the electronic analysis to obtain a second estimate of the velocity and consequently of the spatial properties of the droplets, which however turned out to be a bit biased. By comparing different datasets we also managed to understand how the droplet properties behave as a function of the oil and water fluxes.

The analysis proved to be much more complex than we originally expected when we collected the data, and thus, *a posteriori*, we should have collected data in a different manner, namely at lower fluxes and for longer times. Concerning the hardware it would have been better to have more photocells and a more performing image acquisition system, however, at the end of the day, we were still able to produce some pretty good estimates of the droplet properties.

References

- [1] Piotr Garstecki et al. “Formation of droplets and bubbles in a microfluidic T-junction - Scaling and mechanism of break-up”. In: *Lab on a chip* 6 (Apr. 2006), pp. 437–46. DOI: [10.1039/b510841a](https://doi.org/10.1039/b510841a).
- [2] Todd Thorsen et al. “Dynamic Pattern Formation in Vesicle-Generating Microfluidic Device”. In: *Physical review letters* 86 (May 2001), pp. 4163–6. DOI: [10.1103/PhysRevLett.86.4163](https://doi.org/10.1103/PhysRevLett.86.4163).